Journal of Structural Geology 37 (2012) 105–123

Contents lists available at SciVerse ScienceDirect

Journal of Structural Geology

journal homepage: www.elsevier.com/locate/jsg

Cosserat analysis of interactions between intersecting faults; the wedge faulting

Jure Žalohar

University of Ljubljana, Faculty of Natural Sciences and Engineering, Department of Geology, Aškerčeva 12, SI-1000 Ljubljana, Slovenia

ARTICLE INFO

Article history:
Received 12 March 2011
Received in revised form
15 December 2011
Accepted 24 January 2012
Available online 1 February 2012

Keywords:
Cosserat continuum
Wedge failure
Fault interaction
Fault-slip analysis
Kinematic analysis

ABSTRACT

Classical methods for the fault-slip data analysis generally assume that the slip direction along different faults is independent. However, wedge faulting can often be observed in nature, characterized by the interaction between intersecting faults, which produces a slip direction subparallel to the common intersection direction among the faults. In this article the wedge faulting is described within the frame of the Cosserat theory. We show that this type of faulting is possible both in the classical (Cauchy) continuum as well as in the Cosserat continuum. In the classical continuum, there are two possible optimal interacting subsystems of faults with orientations symmetrically aligned with respect to the kinematic axes of the macrostrain tensor. In the Cosserat continuum these subsystems are not symmetric, because they do not accommodate the same amount of deformation. One of them is dominant and accommodates a larger amount of deformation than the other (weaker) subsystem. In addition, the non-optimal faults with orientations close to the dominant optimal interacting subsystem can also interact, forming an even more complex asymmetric interacting system.

1. Introduction

In the last two decades considerable progress in understanding the effect of block (micro)rotations between the faults was achieved using the Cosserat continuum theory (Twiss et al., 1991, 1993; Twiss and Unruh, 1998, 2007; Figueiredo et al., 2004; Twiss, 2009). The Cosserat continuum belongs to a larger class of generalized continua, which introduce intrinsic length scales into continuum mechanics by accounting for higher order gradients, additional degrees of freedom or fully non-local constitutive equations (e.g., Eringen, 1999, 2002; Forest and Sievert, 2003). While deformation of the classical continuum is described by three independent degrees of freedom (components of the displacement vector), deformation of the Cosserat (or micropolar) continuum is described by three additional degrees of freedom, which are the components of the (micro)rotation vector describing the microrotation of individual segments of the Cosserat continuum. The micropolar theory was proposed in a systematic way by the Cosserat and Cosserat (1909) at the beginning of the 20th century. However, it was only in the last decades that a revival of this theory took place through the milestones presented by, for example, Toupin (1962), Mindlin (1964), Kröner (1968), Eringen and Suhubi (1964), and Eringen (1968), to name a few. These authors also proposed a rigorous set of constitutive and balance equations describing elasticity, hyperelasticity, and viscoelasticity. Nowadays, the Cosserat continuum provides a relevant description of the mechanical behavior of several classes of materials with microstructure, such as liquid crystals, rocks and granular media, cellular solids, composites and dislocated crystals. The pioneering attempts to apply the Cosserat theory in the description of yielding and failure of brittle materials, mechanics of fractured media and localization of plastic deformation of brittle materials, date back to Lippmann (1969), Besdo (1985), and Mühlhaus and Vardoulakis (1987). The Cosserat theory was also successfully applied in the fault-slip data analysis by Twiss et al. (1991, 1993), Twiss and Unruh (1998, 2007), and Figueiredo et al. (2004). These authors were the first to recognize the influence of the block (micro)rotations on fault-slip patterns. In the Cosserat continuum theory, the direction of slip along the faults depends on the Cosserat strain tensor and not on the stress tensor. From this it follows that the patterns of slip along the faults are related in a systematic way to the global deformation.

The theory of kinematics and dynamics of fault reactivation in the Cosserat continuum was further developed by Žalohar and Vrabec (2010), who also derived the constitutive model for stress–strain relationship based on the *J2* plasticity theory. They showed that the strain is not the only parameter affecting the geometry of active fault systems in the Earth's crust. The other parameter is stress. Žalohar and Vrabec (2010) also performed several numerical tests calculating the theoretical slip directions and possible orientations of active faults in a given strain and stress field. The aim of these tests was to discover a relationship between the fault system geometry and the amount of (micro)rotation of

E-mail address: jure.zalohar@guest.arnes.si.

0191-8141/$ – see front matter © 2012 Elsevier Ltd. All rights reserved.
doi:10.1016/j.jsg.2012.01.023

blocks. Their tests indicate that the Cosserat theory spontaneously predicts the slip direction along the faults to be subparallel to their common intersection (wedge faulting). In their article, the authors did not analyze this prediction theoretically.

The aim of this article is to develop a consistent theoretical model of the wedge faulting within the frame of the Cosserat theory. In the first chapter, we summarize some basic ideas of the Cosserat continuum. The meaning of these basic principles is not fully discussed here, therefore the reader should refer to our first article (Žalohar and Vrabec, 2010). In the following chapters, the mathematics behind the interaction between intersecting faults is fully discussed. The theory was tested numerically by the T-TECTO 3.0 computer program (Žalohar and Vrabec, 2007, 2008, 2010) available free of charge at the following site: http://www2.arnes.si/~jzaloh/t-tecto_homepage.htm. T-TECTO solves the inverse problem by minimizing some quantitative measure of misfit between the observed and calculated slip direction along the fault planes, and finds the best-fit of the model parameters to a set of fault-slip data. In this way the T-TECTO computer program finds the stress and strain boundary conditions that explain best the direction of slip along the observed faults. T-TECTO also enables the forward modeling, and calculates the slip direction along the faults in the stress and strain boundary conditions defined by the user. A detailed description of the methods used in the T-TECTO computer program is not given in this article, but can be found in Žalohar and Vrabec (2007, 2008, 2010).

2. Kinematics of the Cosserat continuum

The kinematics of the Cosserat continuum is characterized by a (micro)rotational degree of freedom $\vec{\phi}^{\text{Cosserat}}$, which is independent of the translatory motion described by the displacement field $\vec{u}$ (Fig. 1). In the Cosserat continuum the corresponding strain measures are the *Cosserat strain tensor* $\mathbf{e}$ and the *torsion-curvature tensor* $\boldsymbol{\kappa}$ (Forest, 2000; Forest and Sievert, 2003; Forest et al., 1997, 2000, 2001):

$$\mathbf{e} = \mathbf{u} - \mathbf{W}^C = \vec{u} \otimes \vec{\nabla} + \underline{\varepsilon}\,\vec{\phi}^{\text{Cosserat}} = \frac{\partial u_i}{\partial x_j} + \varepsilon_{ijk}\phi_k^{\text{Cosserat}},$$
$$\boldsymbol{\kappa} = \vec{\phi}^{\text{Cosserat}} \otimes \vec{\nabla} = \frac{\partial \phi_i^{\text{Cosserat}}}{\partial x_j}. \quad (1)$$

Here, $\underline{\varepsilon}$ represents the third-order permutation tensor $\underline{\varepsilon} = \varepsilon_{ijk} = 0.5(i-j)(j-k)(k-i)$, and $\mathbf{W}^C = -\underline{\varepsilon}\,\vec{\phi}^{\text{Cosserat}}$ is the *Cosserat microrotation tensor*, which describes the microrotation of the blocks. We have also introduced the *deformation gradient tensor* (or instantaneous macrodisplacement gradient) $\mathbf{u} = u_{ij} = \partial u_i/\partial x_j = \vec{u} \otimes \vec{\nabla}$. The symmetric part $\mathbf{u}^{(S)}$ of this tensor defines the instantaneous macrostrain, while the skew-symmetric part $\mathbf{u}^{(A)}$ defines the instantaneous macrorotation. The eigenvalues and eigenvectors of the $\mathbf{u}^{(S)}$ are denoted by $\lambda_1, \lambda_2, \lambda_3$ and $\vec{\lambda}_1, \vec{\lambda}_2, \vec{\lambda}_3$. We also take $\lambda_1 \geq \lambda_2 \geq \lambda_3$, where the positive value defines contraction and the negative value defines extension. Note that $\vec{\lambda}_1, \vec{\lambda}_2, \vec{\lambda}_3$ are all unit vectors. In the description of geologic faulting we also take $\mathrm{Tr}(\mathbf{u}^{(S)}) = \lambda_1 + \lambda_2 + \lambda_3 = 0$ (no volume changes), which means that λ_1 is always positive (contraction), whilst λ_3 is always negative (extension). The intermediate eigenvalue λ_2 can be positive or negative.

Because the deformation gradient tensor can be decomposed into the symmetric and skew-symmetric parts $\mathbf{u} = \mathbf{u}^{(S)} + \mathbf{u}^{(A)}$, the Cosserat strain tensor can be written as

$$\mathbf{e} = \mathbf{u}^{(S)} + \mathbf{u}^{(A)} - \mathbf{W}^{(C)} = \mathbf{u}^{(S)} + \mathbf{A}, \quad (2)$$

with $\mathbf{e}^{(S)} = \mathbf{u}^{(S)}$ and $\mathbf{e}^{(A)} = \mathbf{A}$. We have introduced the *relative microrotation tensor*

$$\mathbf{A} = \mathbf{u}^{(A)} - \mathbf{W}^C = \mathbf{W}^{\text{macro}} - \mathbf{W}^C = -\underline{\varepsilon}(\vec{\phi}^{\text{macro}} - \vec{\phi}^{\text{Cosserat}}) = -\underline{\varepsilon}\,\vec{\phi}^{\text{rel}}. \quad (3)$$

The macrorotation or skew-symmetric part of the displacement gradient tensor is $\mathbf{W}^{\text{macro}} = -\underline{\varepsilon}\,\vec{\phi}^{\text{macro}}$, with axial vector $\vec{\phi}^{\text{macro}}$. The difference $(\vec{\phi}^{\text{macro}} - \vec{\phi}^{\text{Cosserat}})$ between the macrorotation and microrotation vectors is here termed the *relative microrotation*. Normally, the Cosserat microrotation vector $\vec{\phi}^{\text{Cosserat}}$ and macrorotation vector $\vec{\phi}^{\text{macro}}$ are axial vectors, which can have any orientation. However, following the simplified model of Twiss et al. (1991, 1993) and Twiss and Unruh (1998, 2007) we presume that both vectors are parallel to the intermediate eigenvector $\vec{\lambda}_2$ of the macrostrain tensor $\mathbf{u}^{(S)}$, because this is likely to be the most significant component. In this case we have $\vec{\phi}^{\text{rel}} = \phi^{\text{rel}}\vec{\lambda}_2$ (Žalohar and Vrabec, 2010).

The magnitude of the relative microrotation is measured by the relative microrotation (or vorticity) parameter (e.g., Twiss and Unruh 1998, 2007)

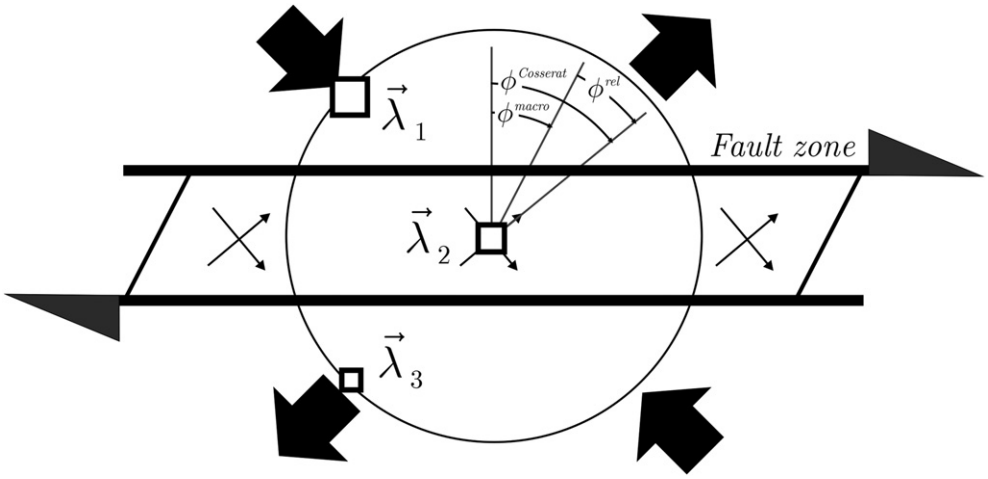

Fig. 1. Micro- and macro-rotations in a Cosserat continuum. $\vec{\phi}^{\text{macro}}$ represents the large-scale regional rotation related to faulting (=axial vector of the deformation gradient tensor). $\vec{\phi}^{\text{Cosserat}}$ is the Cosserat microrotation of individual segments of the Cosserat continuum. $\vec{\phi}^{\text{rel}}$ is the relative microrotation, which is defined as the difference between the macrorotation and the Cosserat microrotation. $\vec{\lambda}_1, \vec{\lambda}_2$ and $\vec{\lambda}_3$ are kinematic axes of the instantaneous deformation tensor.

$$C = \frac{\phi^{\text{macro}} - \phi^{\text{Cosserat}}}{0.5(\lambda_1 - \lambda_3)}. \tag{4}$$

This parameter represents an extra degree of kinematic freedom that describes a normalized measure of the difference between the Cosserat microrotation of the rigid blocks $\vec{\phi}^{\text{Cosserat}}$ and the average macrorotation $\vec{\phi}^{\text{macro}}$ of the global material lines in the global deformation of the rock continuum (Twiss and Unruh, 1998). The denominator in the Eq. (4) is the maximum possible shear strain obtainable from the global macrostrain tensor. In most cases, the value of this parameter ranges from −1 to 1, however, the values $C < -1$ or $C > 1$ are also possible (Twiss et al., 1991, 1993). For $C = 0$, there is no relative microrotation. The sign of C depends on the orientation of the coordinate system, the sense of shear, and the relative magnitudes of microrotation and macrorotation (Twiss et al., 1993; Unruh et al., 1996). Looking in the positive direction along the $\vec{\lambda}_2$ axis, the macrorotation has a right-handed sense about the $\vec{\lambda}_2$ axis for a dextral macroscopic shear. Positive values of C imply that rigid fault-bounded blocks are rotating faster than, and in the same sense as, the macrorotation. Negative values of C, $-1 < C < 0$, imply that the microrotation of the blocks is smaller than the macrorotation of the macroscopic shear zone. $C = -1$ implies the fault blocks do not rotate with respect to the shear zone. Finally, $C < -1$ implies the fault blocks rotate counterclockwise in the shear zone. This last value is possible if there is a component of shortening or lengthening normal to the macroscopic shear zone and the fault blocks have a restricted range of shapes and orientations. Since this situation is unlikely, we do not search for values of C outside the limits $-1 \le C \le 1$ (e.g., Twiss et al., 1993; Unruh et al., 1996). From Eq. (4) we see that the largest absolute value of the relative microrotation is then

$$|C| = 1 \rightarrow \left|\phi^{\text{rel}}_{\max}\right| = \frac{1}{2}(\lambda_1 - \lambda_3). \tag{5}$$

For a sinistral macroscopic shear, the coordinate axes are defined so that the macrorotation has a left-handed sense about the $\vec{\lambda}_2$ axis. In this case the signs of C are reversed. Thus the sign of C does not provide an unique interpretation of the microrotation unless additional independent information, such as the sense of macroscopic shear relative to the positive direction of the $\vec{\lambda}_2$ axis, is available (e.g., Unruh et al., 1996).

Characteristics of the instantaneous macrostrain tensor $\mathbf{u}^{(S)}$ are also described in terms of the instantaneous deformation parameter D

$$D = \frac{(\lambda_2 - \lambda_3)}{(\lambda_1 - \lambda_3)}. \tag{6}$$

This parameter is a scalar invariant of the instantaneous macrostrain tensor $\mathbf{u}^{(S)}$ and defines the shape of the instantaneous strain ellipsoid (e.g., Twiss et al., 1991; Twiss and Unruh, 1998). Its value is unaffected either by the multiplication of each of the principal strains by the same scalar constant or by the addition of any component of volumetric strain rate to the deformation (e.g., Twiss et al., 1991; Twiss and Unruh, 1998) (Table 1).

2.1. The slip direction

The strain and curvature vectors on each microplane (fault) are given by

$$\vec{t}_e = \mathbf{e}\vec{n} = e_{ij}n_j \quad \text{and} \quad \vec{t}_\kappa = \boldsymbol{\kappa}\vec{n} = \kappa_{ij}n_j. \tag{7}$$

The second- and third-order projection tensors $\mathbf{N}$ and $\underline{\mathbf{T}}$ are defined with the fourth-order identity tensor $\underline{\mathbf{1}} = 1_{ijkl} = \delta_{ik}\delta_{jl}$ and the unit normal to the microplane (fault) $\vec{n}$ as (e.g., Etse and Nieto, 2004)

Table 1
Explanation of the most important quantities used in the text.

Symbol	Explanation	First used in Eq.
$\vec{\phi}^{\text{Cosserat}}$	Cosserat microrotation vector	(1)
$\vec{\phi}^{\text{macro}}$	Regional macrorotation vector	(3)
$\vec{\phi}^{\text{rel}}$	Relative microrotation vector	(3)
$\vec{n}$	Unit normal to the fault plane	(7)
$\vec{m}$	Slip direction along the fault	(9)
$\vec{d}$	Director of the interacting system of faults	(42)
C	Relative microrotation parameter	(4)
L	Distance between the centroids of the neighboring blocks measured perpendicular to the fault plane	(9)
p_r, a, b, c and d	Parameters in the constitutive equation for the cataclastic flow	(30)
σ_n and τ	Normal and shear stress along the fault	(12)
$\mathbf{e}$	Cosserat strain tensor	(1)
$\mathbf{e}^{(S)}$ and $\mathbf{e}^{(A)}$	Symmetric and skew-symmetric parts of the Cosserat strain tensor	(2)
$\boldsymbol{\kappa}$	Torsion-curvature tensor	(1)
$\boldsymbol{\sigma}$	Stress tensor	(11)
$\boldsymbol{\mu}$	Couple-stress tensor	(11)
$\underline{\boldsymbol{\varepsilon}}$	Third-order permutation tensor	(1)
$\mathbf{W}^C$	Cosserat microrotation tensor	(2)
$\mathbf{u}$	Deformation gradient tensor	(1)
$\mathbf{u}^{(S)}$	Symmetric part of the deformation gradient tensor (=instantaneous macrostrain tensor)	(2)
$\mathbf{u}^{(A)}$ and $\mathbf{W}^{\text{macro}}$	Skew-symmetric part of the deformation gradient tensor (=instantaneous macrorotation tensor)	(3)
$\mathbf{A}$	Relative microrotation tensor	(3)
$\mathbf{N}$	Second-order projection tensor	(8)
$\underline{\mathbf{T}}$	Third-order projection tensor	(8)
$\underline{\mathbf{1}}$	Fourth-order identity tensor	(8)
$\gamma^s\vec{s} = L\underline{\mathbf{T}} : \mathbf{u}^{(S)}$	Component of slip due to the instantaneous macrostrain	(10)
$\gamma^c\vec{c} = L\underline{\mathbf{T}} : \mathbf{A}$	Component of slip due to the relative microrotation	(10)
$\gamma\vec{m} = L\underline{\mathbf{T}} : \mathbf{e}$	The slip vector along the fault	(9)
$\sigma_n = \mathbf{N} : \boldsymbol{\sigma}$	Normal stress along the fault	(12)
$\vec{\tau} = \underline{\mathbf{T}} : \boldsymbol{\sigma}$	Shear stress vector along the fault	(12)
$a\underline{\mathbf{T}} : \mathbf{u}^{(S)}$	Component of shear stress due to the instantaneous macrostrain	(38)
$b\underline{\mathbf{T}} : \mathbf{A}$	Component of shear stress due to the relative microrotation	(38)

$$\begin{aligned} \mathbf{N} &= \vec{n}\otimes\vec{n} = n_i n_j, \\ \underline{\mathbf{T}} &= \vec{n}\cdot\underline{\mathbf{1}} - \vec{n}\otimes\vec{n}\otimes\vec{n} = n_l 1_{ijkl} - n_i n_j n_k. \end{aligned} \tag{8}$$

In the case of $\boldsymbol{\kappa} = 0$ the direction of slip along the fault is parallel to the resolved shear direction, which is the tangential component of the strain vector

$$\begin{aligned} \gamma\vec{m} &= L\underline{\mathbf{T}} : \mathbf{e} = LT_{ijk}e_{jk} = L(\mathbf{e}\vec{n} - (\mathbf{e}\vec{n}\cdot\vec{n})\vec{n}) \\ &= L(e_{ij}n_j - ((e_{ij}n_j)n_i)n_i). \end{aligned} \tag{9}$$

Here, $\vec{m}$ represents the unit vector in the direction of slip along the fault, γ is the amount of slip, and L is the distance between the centroids of the two neighboring blocks. Because the Cosserat strain tensor depends on the macrodeformation and the relative microrotation tensors, the slip along the fault can be decomposed into two components

$$\gamma\vec{m} = \gamma^s\vec{s} + \gamma^c\vec{c}, \tag{10}$$

where $\gamma^s\vec{s} = L\underline{\mathbf{T}} : \mathbf{u}^{(S)} = LT_{ijk}u^{(S)}_{jk}$ represents the contribution of the macrodeformation field to the slip direction along the fault, while $\gamma^c\vec{c} = L\underline{\mathbf{T}} : \mathbf{A} = LT_{ijk}A_{jk}$ represents the contribution of the relative microrotation.

2.2. The stress measures

Surface forces and couples are represented by the generally non-symmetric tensors, the force-stress tensor $\boldsymbol{\sigma} = \sigma_{ij}$ and the couple-stress tensor $\boldsymbol{\mu} = \mu_{ij}$

$$\vec{\sigma} = \boldsymbol{\sigma}\vec{n} = \sigma_{ij}n_j \quad \text{and} \quad \vec{\mu} = \boldsymbol{\mu}\vec{n} = \mu_{ij}n_j. \tag{11}$$

The force-stress vector and the couple-stress vector can be decomposed into the normal and tangential components

$$\begin{aligned} \sigma_n &= \mathbf{N}:\boldsymbol{\sigma} = N_{ij}\sigma_{ij}, \quad \vec{\tau} = \underline{\mathbf{T}}:\boldsymbol{\sigma} = T_{ijk}\sigma_{jk}, \\ \mu_n &= \mathbf{N}:\boldsymbol{\mu} = N_{ij}\mu_{ij}, \quad \vec{\mu}_t = \underline{\mathbf{T}}:\boldsymbol{\mu} = T_{ijk}\mu_{jk}. \end{aligned} \tag{12}$$

Thus, σ_n and μ_n represent the normal projected stress and the normal projected couple-stress, whereas $\vec{\tau}$ and $\vec{\mu}_t$ represent the shear stress vector and the tangential projected couple-stress vector, respectively.

The force-stress and couple-stress tensors $\boldsymbol{\sigma}$ and $\boldsymbol{\mu}$ must fulfill the equations of balance of momentum and of balance of moment of momentum

$$\begin{aligned} \boldsymbol{\sigma}\cdot\vec{\nabla} + \vec{f} &= \frac{\partial\sigma_{ij}}{\partial x_j} + f_i = 0, \\ \boldsymbol{\mu}\cdot\vec{\nabla} - \underline{\varepsilon}:\boldsymbol{\sigma} + \vec{c} &= \frac{\partial\mu_{ij}}{\partial x_j} - \varepsilon_{ijk}\sigma_{jk} + c_i = 0, \end{aligned} \tag{13}$$

where volume forces $\vec{f}$, volume couples $\vec{c}$, and mass density ρ have been introduced (Forest, 2000).

3. Constitutive equations

Possible characteristics of constitutive equations for the faulting deformations in the Earth's crust (cataclastic flow) were first discussed by Twiss and Unruh (1998). They recognized three principal driving mechanisms that should be incorporated: (1) elastic properties of the blocks bounded by the faults, (2) frictional sliding on the shear surfaces (faults), and (3) plastic deformation and brittle fracture of rocks. The problem was further discussed by Žalohar and Vrabec (2010), who presented the constitutive model based on the *J2* plasticity theory. The authors derived the constitutive equation relating the Cosserat strain tensor to the stress tensor. Here, we summarize their theory and we also discuss the constitutive equation relating the couple-stress and the torsion-curvature tensors. We also present an exact description of the homogeneous Cosserat deformation.

Assuming the strain is small, the Cosserat deformation and torsion-curvature tensors are decomposed into elastic and plastic parts (e.g., Willam, 2002; Forest and Sievert, 2003)

$$\mathbf{e} = \mathbf{e}_e + \mathbf{e}_p, \quad \boldsymbol{\kappa} = \boldsymbol{\kappa}_e + \boldsymbol{\kappa}_p. \tag{14}$$

In the description of the cataclastic flow we assume that $\mathbf{e}_e \ll \mathbf{e}_p$ and $\boldsymbol{\kappa}_e \ll \boldsymbol{\kappa}_p$, so $\mathbf{e} \approx \mathbf{e}_p$ and $\boldsymbol{\kappa} \approx \boldsymbol{\kappa}_p$. As discussed by Forest and Sievert (2003), the classical theory of so-called standard materials proposed by Germain et al. (1983), Lemaitre and Chaboche (1994), and Forest et al. (2001) can be extended to Cosserat media by choosing a viscoplastic potential $\Omega(\boldsymbol{\sigma}, \boldsymbol{\mu}, R)$, the so-called pseudo-potential of dissipation, such that

$$\dot{\mathbf{e}}_p = \frac{\partial\Omega}{\partial\boldsymbol{\sigma}}, \quad \dot{\boldsymbol{\kappa}}_p = \frac{\partial\Omega}{\partial\boldsymbol{\mu}}, \quad \dot{q} = \frac{\partial\Omega}{\partial R}. \tag{15}$$

The thermodynamic force associated with the material internal variable q was denoted by R (see, for example, Forest and Sievert, 2003, for a more detailed definition). For the positivity of the intrinsic dissipation to be ensured, the potential $\Omega(\boldsymbol{\sigma}, \boldsymbol{\mu}, R)$ should be a convex function of its variables.

Two main classes of potentials have been used in the past (Forest and Sievert, 2003). In the first class, the potential is a coupled function of stress and couple-stress tensors, $\Omega(\boldsymbol{\sigma}, \boldsymbol{\mu}, R)$, whereas in the second class the potential is a sum of two independent functions of stress and couple-stress tensors

$$\Omega_{\text{tot}} = \Omega(\boldsymbol{\sigma}, R) + \Omega_c(\boldsymbol{\mu}, R_c). \tag{16}$$

Both classes can be used to describe the rate-independent material behavior. The first class of models involves a single yield function $f(\boldsymbol{\sigma}, \boldsymbol{\mu}, R)$ and a single plastic multiplier $\dot{p}$ (single criterion plasticity model)

$$\dot{\mathbf{e}}_p = \dot{p}\frac{\partial f}{\partial\boldsymbol{\sigma}}, \quad \dot{\boldsymbol{\kappa}}_p = \dot{p}\frac{\partial f}{\partial\boldsymbol{\mu}}, \quad \dot{q} = -\dot{p}\frac{\partial f}{\partial R}. \tag{17}$$

The yielding occurs when $f(\boldsymbol{\sigma}, \boldsymbol{\mu}, R) \le 0$ (the plastic yield condition) (Willam, 2002). The second class of models accounts with two yield functions $f(\boldsymbol{\sigma}, R, R_c)$ and $f_c(\boldsymbol{\mu}, R, R_c)$, and two plastic multipliers (multi-criterion plasticity model)

$$\dot{\mathbf{e}}_p = \dot{p}\frac{\partial f}{\partial\boldsymbol{\sigma}}, \quad \dot{\boldsymbol{\kappa}}_p = \dot{\kappa}\frac{\partial f_c}{\partial\boldsymbol{\mu}}, \quad \dot{q} = -\dot{p}\frac{\partial f}{\partial R}, \quad \dot{q}_c = -\dot{\kappa}\frac{\partial f_c}{\partial R_c}. \tag{18}$$

The yielding occurs when $f(\boldsymbol{\sigma}, R, R_c) \le 0$ and $f_c(\boldsymbol{\mu}, R, R_c) \le 0$. In this last model, the coupling between deformation and curvature comes from the balance equations and possibly coupled hardening laws (Forest and Sievert, 2003). In the literature, numerous yield functions have been proposed, which are mainly modifications and extensions of the Mohr–Coulomb, von Mises and Drucker–Prager yield functions (e.g., de Borst, 1991, 1993; Mohan et al., 1999; Hansen et al., 2001; Manzari, 2004; Salari et al., 2004). The onset of yielding of the Cosserat medium can be successfully accounted for using the extended von Mises or Drucker–Prager yield functions (*J2* plasticity), as discussed, for example, by Sawczuk (1967), Lippmann (1969), Besdo (1974, 1985), Mühlhaus and Vardoulakis (1987), de Borst (1991, 1993), and Forest and Sievert (2003). The following form of the extended von Mises criterion encompasses the models that belong to the class of the single criterion plasticity models

$$f(\boldsymbol{\sigma}, \boldsymbol{\mu}, R) = J_{2d}\left(\boldsymbol{\sigma}^d, \boldsymbol{\mu}\right) - R(p) \tag{19}$$

with

$$J_{2d}\left(\boldsymbol{\sigma}^d, \boldsymbol{\mu}\right) = \sqrt{a_1\boldsymbol{\sigma}^d:\boldsymbol{\sigma}^d + a_2\boldsymbol{\sigma}^d:\boldsymbol{\sigma}^{dT} + b_1\boldsymbol{\mu}:\boldsymbol{\mu} + b_2\boldsymbol{\mu}:\boldsymbol{\mu}^T}. \tag{20}$$

J_{2d} represents the generalized second invariant of deviatoric stress and couple-stress tensors extended to the Cosserat continuum (de Borst, 1993). $\boldsymbol{\sigma}^d$ is the deviatoric part of the stress tensor, $\boldsymbol{\sigma}^{dT}$ is the transposed deviatoric part of the stress tensor, $\boldsymbol{\mu}$ is the couple-stress tensor, $\boldsymbol{\mu}^T$ is the transposed couple-stress tensor, and a_1, a_2, b_1 and b_2 are the material parameters. Note that the stress tensor $\boldsymbol{\sigma}$ can be decomposed into the spherical and deviatoric parts $\boldsymbol{\sigma} = \boldsymbol{\sigma}^{\bigcirc} + \boldsymbol{\sigma}^d$ with $\boldsymbol{\sigma}^{\bigcirc} = \langle\boldsymbol{\sigma}\rangle = (1/3)\text{Tr}(\boldsymbol{\sigma})\mathbf{1}$ and $\boldsymbol{\sigma}^d = \boldsymbol{\sigma} - \boldsymbol{\sigma}^{\bigcirc}$. The trace of the stress tensor $\text{Tr}(\boldsymbol{\sigma})$ is also known as the first invariant J_1 of the stress. From Eq. (17) we have (Forest and Sievert, 2003)

$$\dot{\mathbf{e}}_p = \dot{p}\frac{a_1\boldsymbol{\sigma}^d + a_2\boldsymbol{\sigma}^{dT}}{J_{2d}(\boldsymbol{\sigma}^d, \boldsymbol{\mu})}, \quad \dot{\boldsymbol{\kappa}}_p = \dot{p}\frac{b_1\boldsymbol{\mu} + b_2\boldsymbol{\mu}^T}{J_{2d}(\boldsymbol{\sigma}^d, \boldsymbol{\mu})}, \tag{21}$$

The use of the consistency condition $\dot{f} = 0$ for plastic loading leads to the following expression for the plastic multiplier (Forest and Sievert, 2003)

$$\dot{p}=\sqrt{\frac{a_1}{a_1^2-a_2^2}\dot{\mathbf{e}}_p:\dot{\mathbf{e}}_p+\frac{a_2}{a_2^2-a_1^2}\dot{\mathbf{e}}_p:\dot{\mathbf{e}}_p^T+\frac{b_1}{b_1^2-b_2^2}\dot{\boldsymbol{\kappa}}_p:\dot{\boldsymbol{\kappa}}_p+\frac{b_2}{b_2^2-b_1^2}\dot{\boldsymbol{\kappa}}_p:\dot{\boldsymbol{\kappa}}_p^T}. \tag{22}$$

This is, however, not the only possible extension of the von Mises plasticity since the multi-criterion framework can also be adopted (Forest and Sievert, 2003)

$$\begin{aligned} f(\boldsymbol{\sigma},R) &= J_{2d}\left(\boldsymbol{\sigma}^d\right)-R(p,\kappa),\\ f_c(\boldsymbol{\mu},R_c) &= J_{2d}(\boldsymbol{\mu})-R_c(p,\kappa). \end{aligned} \tag{23}$$

Here, $J_{2d}(\boldsymbol{\sigma}^d)$ and $J_{2d}(\boldsymbol{\mu})$ are as follows:

$$\begin{aligned} J_{2d}\left(\boldsymbol{\sigma}^d\right) &= \sqrt{a_1\boldsymbol{\sigma}^d:\boldsymbol{\sigma}^d+a_2\boldsymbol{\sigma}^d:\boldsymbol{\sigma}^{dT}},\\ J_{2d}(\boldsymbol{\mu}) &= \sqrt{b_1\boldsymbol{\mu}:\boldsymbol{\mu}+b_2\boldsymbol{\mu}:\boldsymbol{\mu}^T}. \end{aligned} \tag{24}$$

The use of the consistency conditions $\dot{f}=0$ and $\dot{f}_c=0$ for plastic loading leads to the following expressions for the two distinct plastic multipliers (Forest and Sievert, 2003):

$$\begin{aligned} \dot{p} &= \sqrt{\frac{a_1}{a_1^2-a_2^2}\dot{\mathbf{e}}_p:\dot{\mathbf{e}}_p+\frac{a_2}{a_2^2-a_1^2}\dot{\mathbf{e}}_p:\dot{\mathbf{e}}_p^T},\\ \dot{\kappa} &= \sqrt{\frac{b_1}{b_1^2-b_2^2}\dot{\boldsymbol{\kappa}}_p:\dot{\boldsymbol{\kappa}}_p+\frac{b_2}{b_2^2-b_1^2}\dot{\boldsymbol{\kappa}}_p:\dot{\boldsymbol{\kappa}}_p^T}. \end{aligned} \tag{25}$$

The flow rules (Eq. (18)) then read

$$\dot{\mathbf{e}}_p=\dot{p}\frac{a_1\boldsymbol{\sigma}^d+a_2\boldsymbol{\sigma}^{dT}}{J_{2d}(\boldsymbol{\sigma}^d)},\quad \dot{\boldsymbol{\kappa}}_p=\dot{\kappa}\frac{b_1\boldsymbol{\mu}+b_2\boldsymbol{\mu}^T}{J_{2d}(\boldsymbol{\mu})}, \tag{26}$$

The constitutive equations that relate the stress and couple-stress tensors to the Cosserat strain and torsion-curvature tensors can be derived from Eq. (21) and/or Eq. (26). For example, Eq. (26) can be rewritten into the following form:

$$\begin{aligned} \dot{\mathbf{e}}_p &= \frac{\dot{p}}{J_{2d}(\boldsymbol{\sigma}^d)}(a_1+a_2)\ \boldsymbol{\sigma}^{(\mathrm{S},d)}+\frac{\dot{p}}{J_{2d}(\boldsymbol{\sigma}^d)}(a_1-a_2)\boldsymbol{\sigma}^{(\mathrm{A},d)},\\ \dot{\boldsymbol{\kappa}}_p &= \frac{\dot{\kappa}}{J_{2d}(\boldsymbol{\mu})}(b_1+b_2)\ \boldsymbol{\mu}^{(\mathrm{S})}+\frac{\dot{\kappa}}{J_{2d}(\boldsymbol{\mu})}(b_1-b_2)\boldsymbol{\mu}^{(\mathrm{A})}. \end{aligned} \tag{27}$$

where $\boldsymbol{\sigma}^{(\mathrm{S},d)}$ is the symmetric part of the stress deviator, $\boldsymbol{\sigma}^{(\mathrm{A},d)}$ is the skew-symmetric part of the stress deviator, $\boldsymbol{\mu}^{(\mathrm{S})}$ is the symmetric part of the couple-stress tensor, and $\boldsymbol{\mu}^{(\mathrm{A})}$ is the skew-symmetric part of the couple-stress tensor. From these equations it also follows:

$$\begin{aligned} \dot{\mathbf{e}}_p^{(\mathrm{S})} &= \frac{\dot{p}}{J_{2d}(\boldsymbol{\sigma}^d)}(a_1+a_2)\boldsymbol{\sigma}^{(\mathrm{S},d)},\\ \dot{\mathbf{e}}_p^{(\mathrm{A})} &= \frac{\dot{p}}{J_{2d}(\boldsymbol{\sigma}^d)}(a_1-a_2)\boldsymbol{\sigma}^{(\mathrm{A},d)},\\ \dot{\boldsymbol{\kappa}}_p^{(\mathrm{S})} &= \frac{\dot{\kappa}}{J_{2d}(\boldsymbol{\mu})}(b_1+b_2)\boldsymbol{\mu}^{(\mathrm{S})},\\ \dot{\boldsymbol{\kappa}}_p^{(\mathrm{A})} &= \frac{\dot{\kappa}}{J_{2d}(\boldsymbol{\mu})}(b_1-b_2)\boldsymbol{\mu}^{(\mathrm{A})}. \end{aligned} \tag{28}$$

Note that $\dot{f}=0$ and $\dot{f}_c=0$, which means that $J_{2d}(\boldsymbol{\sigma}^d)=R(p,\kappa)$ and $J_{2d}(\boldsymbol{\mu})=R_c(p,\kappa)$ (see Eq. (23)). The deviatoric part of the stress tensor and the couple-stress tensor are then

$$\begin{aligned} \boldsymbol{\sigma}^d &= \boldsymbol{\sigma}^{(\mathrm{S},d)}+\boldsymbol{\sigma}^{(\mathrm{A},d)}=\frac{R(p,\kappa)}{\dot{p}(a_1+a_2)}\dot{\mathbf{e}}_p^{(\mathrm{S})}+\frac{R(p,\kappa)}{\dot{p}(a_1-a_2)}\dot{\mathbf{e}}_p^{(\mathrm{A})},\\ \boldsymbol{\mu} &= \boldsymbol{\mu}^{(\mathrm{S})}+\boldsymbol{\mu}^{(\mathrm{A})}=\frac{R_c(p,\kappa)}{\dot{\kappa}(b_1+b_2)}\dot{\boldsymbol{\kappa}}_p^{(\mathrm{S})}+\frac{R_c(p,\kappa)}{\dot{\kappa}(b_1-b_2)}\dot{\boldsymbol{\kappa}}_p^{(\mathrm{A})}. \end{aligned} \tag{29}$$

The constitutive equation relating the Cosserat strain tensor to the full stress tensor can be formulated by adding the hydrostatic pressure term $p_r\mathbf{1}$

$$\begin{aligned} \boldsymbol{\sigma} &= p_r\mathbf{1}+a\dot{\mathbf{e}}_p^{(\mathrm{S})}+b\dot{\mathbf{e}}_p^{(\mathrm{A})},\\ \boldsymbol{\mu} &= c\dot{\boldsymbol{\kappa}}_p^{(\mathrm{S})}+d\dot{\boldsymbol{\kappa}}_p^{(\mathrm{A})}, \end{aligned} \tag{30}$$

with $a=R(p,\kappa)/\dot{p}(a_1+a_2)$, $b=R(p,\kappa)/\dot{p}(a_1-a_2)$, $c=R_c(p,\kappa)/\dot{\kappa}(b_1+b_2)$, and $d=R_c(p,\kappa)/\dot{\kappa}(b_1-b_2)$ as the constitutive parameters. It is important that the same form of the constitutive relations as in Eq. (29) and/or Eq. (30) can also be derived for the single criterion plasticity model (Eq. (21)) and for other yield functions within the *J2* plasticity theory, for example, for the Drucker–Prager yield function (see, for example, de Borst, 1993, and Hansen et al., 2001, for the definition) and for the Pitman–Schaeffer–Gray–Stiles yield function (Dartevelle, 2003).

3.1. Description of the homogeneous Cosserat deformation

Looking at the definition of the Cosserat deformation measures (Eq. (1)) it appears that the torsion-curvature tensor is uniquely determined by the gradient of the Cosserat strain tensor (Toupin, 1962, 1964; Forest and Sievert, 2003)

$$\begin{aligned} \boldsymbol{\kappa}_p &= \frac{1}{2}\underline{\varepsilon}:\left(\mathbf{e}_p\otimes\vec{\nabla}\ +\vec{\nabla}\otimes\left(\mathbf{e}_p+\mathbf{e}_p^T\right)\right)\\ &= \frac{1}{2}\varepsilon_{lij}\left(e_{ij,k}+\left(e_{jk}+e_{kj}\right)_{,i}\right). \end{aligned} \tag{31}$$

If the gradient of the Cosserat strain tensor is equal to zero, the torsion-curvature tensor is also equal to zero

$$\mathbf{e}_p\otimes\vec{\nabla}\ =0\rightarrow\boldsymbol{\kappa}_p=\vec{\phi}^{\mathrm{Cosserat}}\otimes\vec{\nabla}\ =0 \tag{32}$$

These two expressions define the homogeneous Cosserat deformation field. In the terms of the rates-of-deformation this also means that $\dot{\boldsymbol{\kappa}}_p=\dot{\vec{\phi}}^{\mathrm{Cosserat}}\otimes\vec{\nabla}\ =0$. Note that in the Cosserat media the torsion-curvature tensor $\boldsymbol{\kappa}_p$ is not related to the relative microrotation but to the differential changes of the microrotations in the neighborhood of a point. The above equation also shows that if the torsion-curvature tensor $\boldsymbol{\kappa}_p$ is zero, then the gradient of the Cosserat strain tensor is just the gradient of the symmetric part of the Cosserat strain, which does not need to be zero. So the deformation can be inhomogeneous even if $\boldsymbol{\kappa}_p=0$. Thus, $\boldsymbol{\kappa}_p=0$ is a necessary but not a sufficient condition for the homogeneous deformation.

It follows from the constitutive equations (Eq. (30)) that in the homogeneous Cosserat deformation field the couple-stress tensor is equal to zero

$$\dot{\boldsymbol{\kappa}}_p=0\rightarrow\boldsymbol{\mu}=c\dot{\boldsymbol{\kappa}}_p^{(\mathrm{S})}+d\dot{\boldsymbol{\kappa}}_p^{(\mathrm{A})}=0. \tag{33}$$

This is a very important result. We could expect that the couple-stress tensor is related to the relative microrotation, but it is not. The couple-stress tensor is related to the gradient of the Cosserat microrotation, $\boldsymbol{\kappa}_p=\vec{\phi}^{\mathrm{Cosserat}}\otimes\vec{\nabla}$. In the homogeneous Cosserat deformation field the couple-stress tensor is equal to zero even when the relative microrotation is large. Relative microrotation is not necessarily related to some actual (micro)rotation of blocks bounded by the fault planes. The relative microrotation is the difference between the (regional) macrorotation and the microrotation of the blocks. Even when the microrotation of blocks is equal to zero, the macrorotation can be large. Consequently, the relative microrotation is also large. One such example is the case of the simple shear, where the sliding along numerous parallel faults is accompanied by non-zero macrorotation and relative

microrotation even if the actual microrotation of blocks between the parallel faults is equal to zero.

In summary, in the homogeneous Cosserat deformation field the torsion-curvature tensor $\boldsymbol{\kappa}_p$ and couple-stress tensor $\boldsymbol{\mu}$ are supposed to be small. This means that $\boldsymbol{\kappa}_p \approx 0$, $\boldsymbol{\mu} \approx 0$, and also $\boldsymbol{\mu}\cdot\nabla \approx 0$. In this case the skew-symmetric part of the stress tensor is only balanced by the volume couples $\vec{c}$ (see Eq. (13)). We have two examples:

1. If the volume couples $\vec{c}$ are small, the skew-symmetric part of the stress tensor is also small and the stress state is symmetric. It follows that we may have situations with intensive relative microrotation accompanied by symmetric stress state. Three conditions must be fulfilled in this case; (1) constant rate-of-strain, (2) homogeneous Cosserat deformation, and (3) body couples are absent. In this case the actual microrotation of blocks between the fault planes is zero and the relative microrotation would only be the consequence of the macrorotation.
2. In the second case of homogeneous Cosserat deformation and high volume couples we can expect an asymmetric stress state. Because we suppose the electromagnetic or other forces (with the exception of the gravity force) in the Earth's crust are not high enough to influence tectonic faulting and rotations of the blocks, the volume couples can only be related to the gravity force acting on asymmetric blocks bounded by the fault planes. We may presume that the volume couples would be high in the case of highly asymmetric blocks with the mass center not aligned with the center of (micro)rotation.

In effect, the above discussion shows (1) that the "symmetric classical stress state" can be associated with a relative microrotation and (2) that the motions associated with the extra degree of freedom in a Cosserat material (=relative microrotation) are not necessarily associated with any asymmetric stresses or couple-stresses in the material.

3.2. Elimination of the time

Because in the homogeneous Cosserat deformation field the torsion-curvature tensor $\boldsymbol{\kappa}_p$ and the couple-stress tensor $\boldsymbol{\mu}$ are equal to zero, we only have one constitutive equation relating the Cosserat strain tensor $\mathbf{e}_p$ and the stress tensor $\boldsymbol{\sigma}$

$$\boldsymbol{\sigma} = p_r\mathbf{1} + a\dot{\mathbf{e}}_p^{(\mathrm{S})} + b\dot{\mathbf{e}}_p^{(\mathrm{A})}. \tag{34}$$

Although this constitutive relation is formulated in terms of rates-of-deformation, in practice, we interpret these rates to be represented by small increments of deformation that accumulate over a finite but geologically very short time interval (e.g., Twiss and Unruh, 2007). Supposing that the rate-of-deformation was approximately constant during the deformation phase, the time could be eliminated from the constitutive equation by multiplying the Eq. (30) by Δt, which does not affect the result. Thus, the rates are represented by the instantaneous deformation, and the time interval over which these increments accumulate is not a factor in the analysis. In the fault-slip data analysis the Cosserat strain and the corresponding stress tensors of the form $\mathbf{e} = \mathrm{const.}\mathbf{e}^{(\mathrm{orig.})}$ and $\boldsymbol{\sigma} = \mathrm{const.}\boldsymbol{\sigma}^{(\mathrm{orig.})}$ are generally calculated. Here, $\mathbf{e}^{(\mathrm{orig.})}$ and $\boldsymbol{\sigma}^{(\mathrm{orig.})}$ are the actual Cosserat strain and corresponding stress tensors at the time of faulting and $\mathbf{e}$ and $\boldsymbol{\sigma}$ are our solutions, while const. is some undetermined constant. The constitutive equation (Eq. (34)) then reads

$$\boldsymbol{\sigma} = p_r\mathbf{1} + a\mathbf{e}_p^{(\mathrm{S})} + b\mathbf{e}_p^{(\mathrm{A})} = p_r\mathbf{1} + a\mathbf{u}^{(\mathrm{S})} + b\mathbf{A}. \tag{35}$$

Note that we also take $\mathbf{e}_p \approx \mathbf{e} = \mathbf{u}^{(\mathrm{S})} + \mathbf{A}$ and $\boldsymbol{\kappa} \approx \boldsymbol{\kappa}_p$.

3.3. The state of stress along the faults in the homogeneous Cosserat deformation field

The form of the constitutive equation used in the T-TECTO computer program is

$$\boldsymbol{\sigma} = (1-b)T\cdot 1 + (1-b)\mathbf{u}^{(\mathrm{S})} + b\mathbf{A} \tag{36}$$

Because the tensors of the form $\boldsymbol{\sigma} = \mathrm{const.}\boldsymbol{\sigma}^{(\mathrm{orig.})}$ and $\mathbf{e} = \mathrm{const.}\mathbf{e}^{(\mathrm{orig.})}$ are only determined in the fault-slip data analysis, we may take $a + b = 1$. In addition, the first parameter p_r on the right side of Eq. (36) is defined as $(1-b)T$, with T being a parameter related to the hydrostatic pressure. In this way, the stress tensor $\boldsymbol{\sigma}$ is proportional to the Cosserat strain tensor $\mathbf{e}$, when we choose $b = 0.5$

$$\boldsymbol{\sigma} = (1-b)\left(T\mathbf{1} + \mathbf{u}^{(\mathrm{S})} + \frac{b}{1-b}\mathbf{A}\right) = \frac{1}{2}\left(T\mathbf{1} + \mathbf{u}^{(\mathrm{S})} + \mathbf{A}\right) = \frac{1}{2}(T\mathbf{1} + \mathbf{e}). \tag{37}$$

It follows from the equations $\gamma\vec{m} = L\underline{\mathbf{T}}:\mathbf{e}$ and $\vec{\tau} = \underline{\mathbf{T}}:\boldsymbol{\sigma} = 1/2(T\underline{\mathbf{T}}:1 + \underline{\mathbf{T}}:\mathbf{e}) = 1/2(\underline{\mathbf{T}}:\mathbf{e})$ that in this case the shear stress and the slip direction are parallel. Note that $\underline{\mathbf{T}}:\mathbf{1} = 0$.

From the linear constitutive law (Eq. (35)) we can derive the following equations for the normal stress and the shear stress vector:

$$\begin{aligned} \sigma_n &= \mathbf{N}:\boldsymbol{\sigma} = p_r\mathbf{N}:\mathbf{1} + a\mathbf{N}:\mathbf{u}^{(\mathrm{S})} + b\mathbf{N}:\mathbf{A} = p_r\mathbf{N}:\mathbf{1} + a\mathbf{N}:\mathbf{u}^{(\mathrm{S})}, \\ \vec{\tau} &= \underline{\mathbf{T}}:\boldsymbol{\sigma} = p_r\underline{\mathbf{T}}:\mathbf{1} + a\underline{\mathbf{T}}:\mathbf{u}^{(\mathrm{S})} + b\underline{\mathbf{T}}:\mathbf{A} = a\underline{\mathbf{T}}:\mathbf{u}^{(\mathrm{S})} + b\underline{\mathbf{T}}:\mathbf{A}, \end{aligned} \tag{38}$$

where $b\mathbf{N}:\mathbf{A} = 0$ (=component of the normal stress due to the relative microrotation) and $p_r\underline{\mathbf{T}}:\mathbf{1} = 0$ (=component of the shear stress due to the hydrostatic pressure). The component of shear stress due to the instantaneous macrodeformation is $a\underline{\mathbf{T}}:\mathbf{u}^{(\mathrm{S})}$, and the component of shear stress due to the relative microrotation is $b\underline{\mathbf{T}}:\mathbf{A}$.

3.4. Fault reactivation

Because of the nonlinear constitutive relationship between the stress and strain, the shear stress $\vec{\tau} = \underline{\mathbf{T}}:\boldsymbol{\sigma}$ is generally non-parallel to the direction of movement. The direction of slip along the fault is given by equation $\gamma\vec{m} = L\underline{\mathbf{T}}:\mathbf{e}$ and depends on the Cosserat strain tensor (supposing that the torsion-curvature tensor can be neglected). In addition, the traction of the two neighboring blocks is also related to a couple-stress, with a normal component μ_n=$\mathbf{N}$:$\boldsymbol{\mu}$ and a tangential component $\vec{\mu}_t = \underline{\mathbf{T}}:\boldsymbol{\mu}$. Generalization of the Amontons' condition to the Cosserat continuum would be (Žalohar and Vrabec, 2010)

$$\left(\vec{\tau} + \frac{1}{L_c}\vec{\mu}_t\right)\cdot\vec{m} \geq \mu\left(\sigma_n + \frac{1}{L_c}\mu_n\right) \tag{39}$$

or

$$\left(\underline{\mathbf{T}}:\boldsymbol{\sigma} + \frac{1}{L_c}\underline{\mathbf{T}}:\boldsymbol{\mu}\right)\cdot\vec{m} \geq \mu\left(\mathbf{N}:\boldsymbol{\sigma} + \frac{1}{L_c}\mathbf{N}:\boldsymbol{\mu}\right). \tag{40}$$

Here L_c represents characteristic length for the torsion-curvature in the Cosserat medium, and μ is the friction coefficient. In some cases we expect that L_c could be of the same order of magnitude than the distance of the centroids of the two neighboring blocks L. In the case of homogeneous deformation of the Cosserat medium, the

torsion-curvature tensor $\boldsymbol{\kappa}$ remains small, because it depends on the gradient of the Cosserat strain tensor $\mathbf{e}$ (Žalohar and Vrabec, 2010). From the constitutive equations (Eq. (30)) it follows that the couple-stress tensor is also small, which means that the couple-stress $\boldsymbol{\mu}$ and characteristic length L_c in the Eq. (40) can be neglected. In this case the condition for fault reactivation depends only on the stress tensor $\boldsymbol{\sigma}$ (Amontons' law of friction)

$$(\underline{\mathbf{T}} : \boldsymbol{\sigma}) \cdot \vec{m} \geq \mu \mathbf{N} : \boldsymbol{\sigma} \text{ or } \tau^r = \vec{\tau} \cdot \vec{m} \geq \mu \sigma_n. \tag{41}$$

This equation assumes that only the faults on which the shear stress exceeds the frictional shear strength can be active. The probability for a fault to slip is often described also in terms of the driving shear stress in the direction of movement, $\vec{\tau} \cdot \vec{m} - \mu\sigma_n$, which should be as high as possible (e.g., Žalohar and Vrabec, 2008).

4. Interaction between intersecting faults

In the wedge failure, the interacting system of faults consists of at least two intersecting faults having direction of movement subparallel to the common intersection direction (Fig. 2). Take two faults with the unit normals $\vec{n}_1$ and $\vec{n}_2$. The distances between adjacent block centroids measured perpendicular to the fault planes are L_1 and L_2. The director (intersection vector) is

$$\vec{d} = (\vec{n}_1 \times \vec{n}_2)/\|(\vec{n}_1 \times \vec{n}_2)\|. \tag{42}$$

The shear (movement) direction should be parallel to $\vec{d}$

$$\begin{aligned} \dot{\gamma}\vec{d} &= L_1(\dot{\mathbf{e}}\vec{n}_1 - (\dot{\mathbf{e}}\vec{n}_1 \cdot \vec{n}_1)\vec{n}_1) = \dot{\gamma}_1^s \vec{s}_1 + \dot{\gamma}_1^c \vec{c}_1, \\ \dot{\gamma}\vec{d} &= L_2(\dot{\mathbf{e}}\vec{n}_2 - (\dot{\mathbf{e}}\vec{n}_2 \cdot \vec{n}_2)\vec{n}_2) = \dot{\gamma}_2^s \vec{s}_2 + \dot{\gamma}_2^c \vec{c}_2. \end{aligned} \tag{43}$$

We are looking for the solutions that satisfy this slip condition. Note that the above and all the following equations are written in terms of the slip velocity. By setting the right sides of the Eq. (43) equal, it follows that,

$$\dot{\gamma}_1^s \vec{s}_1 - \dot{\gamma}_2^s \vec{s}_2 = -\left(\dot{\gamma}_1^c \vec{c}_1 - \dot{\gamma}_2^c \vec{c}_2\right). \tag{44}$$

Because $\dot{\gamma}^c \vec{c} = L\dot{\vec{\phi}}^{\text{rel}} \times \vec{n}$, we have

$$\dot{\gamma}_1^s \vec{s}_1 - \dot{\gamma}_2^s \vec{s}_2 = -\dot{\vec{\phi}}^{\text{rel}} \times (L_1 \vec{n}_1 - L_2 \vec{n}_2), \tag{45}$$

or in a more simple form

$$\Delta\dot{\vec{s}} = -\dot{\vec{\phi}}^{\text{rel}} \times \Delta\vec{n}, \tag{46}$$

with $\Delta\dot{\vec{s}} = \dot{\gamma}_1^s \vec{s}_1 - \dot{\gamma}_2^s \vec{s}_2$ and $\Delta\vec{n} = L_1\vec{n}_1 - L_2\vec{n}_2$, where $\Delta\vec{n}$ is no longer an unit vector. Note that $\dot{\gamma}^s \vec{s} = L\underline{\mathbf{T}} : \dot{\mathbf{u}}^{(S)}$. Therefore, Eq. (46) can be written as

$$\left(\underline{\mathbf{T}}_1 - \frac{L_2}{L_1}\underline{\mathbf{T}}_2\right) : \dot{\mathbf{u}}^{(S)} = -\dot{\vec{\phi}}^{\text{rel}} \times \left(\vec{n}_1 - \frac{L_2}{L_1}\vec{n}_2\right). \tag{47}$$

The rate-of-relative microrotation is $\dot{\phi}^{\text{rel}} = \Delta\dot{s}/(\Delta n \sin\alpha)$, where α is the angle between $\dot{\vec{\phi}}^{\text{rel}}$ and $\Delta\vec{n}$. The two vectors $\Delta\vec{n}$ and $\Delta\dot{\vec{s}}$ have the components $(\Delta n_1, \Delta n_2, \Delta n_3)$ and $(\Delta\dot{s}_1, \Delta\dot{s}_2, \Delta\dot{s}_3)$. We see from Eq. (47) that the rate-of-relative microrotation linearly depends on the rate-of-macrostrain $\dot{\mathbf{u}}^{(S)}$.

The above Eq. (46) can be rewritten into the following form:

$$\Delta\dot{\vec{s}} = \mathbf{G}\dot{\vec{\phi}}^{\text{rel}}, \tag{48}$$

with

$$\mathbf{G} = \begin{bmatrix} 0 & \Delta n_3 & -\Delta n_2 \\ -\Delta n_3 & 0 & \Delta n_1 \\ \Delta n_2 & -\Delta n_1 & 0 \end{bmatrix}. \tag{49}$$

Note that $\mathbf{G}$ is a singular operator. The rate-of-relative microrotation $\dot{\vec{\phi}}^{\text{rel}}$ can be written in the coordinate system defined by the base vectors $\Delta\vec{n}/\Delta n$ and $(\Delta\vec{n} \times \Delta\dot{\vec{s}})/\|\Delta\vec{n} \times \Delta\dot{\vec{s}}\|$ in the following form:

$$\begin{aligned} \dot{\vec{\phi}}^{\text{rel}} &= \frac{\Delta\dot{s}}{\Delta n}\left[\frac{\Delta\vec{n}}{\Delta n} ctg\alpha + \frac{\Delta\vec{n} \times \Delta\dot{\vec{s}}}{\|\Delta\vec{n} \times \Delta\dot{\vec{s}}\|}\right] \quad \text{and} \\ \dot{\mathbf{A}} &= -\underline{\varepsilon}\dot{\vec{\phi}}^{\text{rel}} = \dot{\mathbf{A}}(\dot{\mathbf{u}}^{(S)}, \alpha). \end{aligned} \tag{50}$$

Based on this equation, the rate-of-relative microrotation $\dot{\vec{\phi}}^{\text{rel}}$ is a function of the rate-of-macrostrain tensor $\dot{\mathbf{u}}^{(S)}$ and the angle α between the vectors $\Delta\vec{n}$ and $\dot{\vec{\phi}}^{\text{rel}}$. From Eq. (50) we get

$$\begin{aligned} \dot{\vec{\phi}}^{\text{rel}} &= \dot{\beta}_1 \Delta\vec{n} \cdot ctg\alpha + \dot{\beta}_2 \Delta\vec{n} \times \Delta\dot{\vec{s}}, \\ \dot{\beta}_1 &= \frac{\Delta\dot{s}}{\Delta n^2} \text{ and } \dot{\beta}_2 = \frac{\Delta\dot{s}}{\|\Delta\vec{n} \times \Delta\dot{\vec{s}}\|\Delta n} \end{aligned} \tag{51}$$

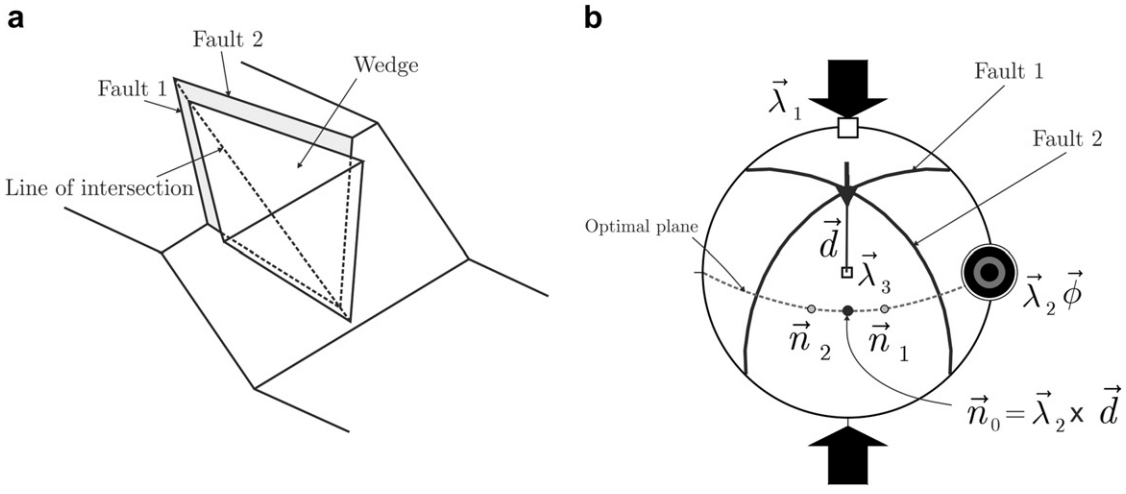

Fig. 2. Schematic illustration of wedge faulting (simplified after Yoon et al., 2002). (a) Sliding direction is parallel to the line of intersection among two faults. (b) Stereographic projection. $\vec{\lambda}_1, \vec{\lambda}_2, \vec{\lambda}_3$ – kinematic axes of the instantaneous deformation tensor, $\vec{n}_1, \vec{n}_2$ – unit normals to faults 1 and 2, $\vec{\phi}$ – relative microrotation vector parallel to $\vec{\lambda}_2$. In this case the relative microrotation has the contra-clockwise direction around the $\vec{\lambda}_2$ axis, which is marked with $\odot$. These same symbols marking the principal macrostrain axes are also used in the diagrams in the subsequent figures.

and

$$\dot{\vec{\phi}}^{\mathrm{rel}} = \dot{\beta}_1 \Delta\vec{n}\cdot ctg\alpha + \dot{\beta}_2 \mathbf{G}\Delta\dot{\vec{s}}. \tag{52}$$

The geometry of the intersecting faults does not define the angle α. Its value can only be defined by the dissipation energy. Because $\mathbf{G}$ is a singular operator, expressing $\dot{\vec{\phi}}^{\mathrm{rel}}$ requires some mathematical manipulation. In our highly simplified case of homogeneous deformation field (supposing that torsion-curvature tensor $\boldsymbol{\kappa}$ can be neglected) the rate-of-dissipation of energy can be written as (see Forest and Sievert, 2003)

$$\dot{D}(\dot{\mathbf{u}}^{(S)},\alpha) = \boldsymbol{\sigma}:\dot{\mathbf{e}} = (p_r\mathbf{1} + a\dot{\mathbf{u}}^{(S)} + b\dot{\mathbf{A}}) : (\dot{\mathbf{u}}^{(S)} + \dot{\mathbf{A}}). \tag{53}$$

The angle α is defined by

$$\frac{\partial\dot{D}}{\partial\alpha} = 0. \tag{54}$$

Because $p_r\mathbf{1} + a\dot{\mathbf{u}}^{(S)}$ does not depend on α, we have

$$\frac{\partial}{\partial\alpha}\dot{D} = \frac{\partial}{\partial\alpha}\boldsymbol{\sigma}:\dot{\mathbf{e}} + \boldsymbol{\sigma}:\frac{\partial}{\partial\alpha}\dot{\mathbf{e}} = \frac{\partial}{\partial\alpha}b\dot{\mathbf{A}}:\dot{\mathbf{e}} + \boldsymbol{\sigma}:\frac{\partial}{\partial\alpha}\dot{\mathbf{A}}. \tag{55}$$

where

$$\frac{\partial}{\partial\alpha}b\dot{\mathbf{A}}:\dot{\mathbf{e}} = b\dot{\beta}_1\frac{1}{\sin^2\alpha}(\underline{\varepsilon}\cdot\Delta\vec{n}) : \dot{\mathbf{u}}^{(S)} - b\dot{\beta}_1^2\frac{\cos\alpha}{\sin^3\alpha}(\underline{\varepsilon}\cdot\Delta\vec{n}) : (\underline{\varepsilon}\cdot\Delta\vec{n}) - b\dot{\beta}_1\dot{\beta}_2\frac{1}{\sin^2\alpha}(\underline{\varepsilon}\cdot\Delta\vec{n}) : (\mathbf{G}\cdot(\underline{\varepsilon}\cdot\Delta\dot{\vec{s}})) \tag{56}$$

and

$$\boldsymbol{\sigma}:\frac{\partial}{\partial\alpha}\dot{\mathbf{A}} = p_r\dot{\beta}_1\frac{1}{\sin^2\alpha}\mathbf{1} : (\underline{\varepsilon}\cdot\Delta\vec{n}) + a\dot{\beta}_1\frac{1}{\sin^2\alpha}\dot{\mathbf{u}}^{(S)} : (\underline{\varepsilon}\cdot\Delta\vec{n}) - b\dot{\beta}_1^2\frac{\cos\alpha}{\sin^3\alpha}(\underline{\varepsilon}\cdot\Delta\vec{n}) : (\underline{\varepsilon}\cdot\Delta\vec{n}) - b\dot{\beta}_1\dot{\beta}_2\frac{1}{\sin^2\alpha}((\underline{\varepsilon}\cdot(G\cdot\Delta\dot{\vec{s}})) : (\underline{\varepsilon}\cdot\Delta\vec{n})). \tag{57}$$

Having these expressions in mind, we can now combine all terms with $1/\sin^2\alpha$ and all terms with $\cos\alpha/\sin^3\alpha$ in Eq. (55). We get the following:

$$\frac{\partial}{\partial\alpha}\dot{D} = A\frac{1}{\sin^2\alpha} - B\frac{\cos\alpha}{\sin^3\alpha} = 0, \tag{58}$$

where

$$A = b\dot{\beta}_1(\underline{\varepsilon}\cdot\Delta\vec{n}) : \dot{\mathbf{u}}^{(S)} - b\dot{\beta}_1\dot{\beta}_2(\underline{\varepsilon}\cdot\Delta\vec{n}) : (\mathbf{G}\cdot(\underline{\varepsilon}\cdot\Delta\dot{\vec{s}})) + p_r\dot{\beta}_1\mathbf{1} : (\underline{\varepsilon}\cdot\Delta\vec{n}) + a\dot{\beta}_1\dot{\mathbf{u}}^{(S)} : (\underline{\varepsilon}\cdot\Delta\vec{n}) - b\dot{\beta}_1\dot{\beta}_2(\underline{\varepsilon}\cdot(\mathbf{G}\cdot\Delta\dot{\vec{s}})) : (\underline{\varepsilon}\cdot\Delta\vec{n}) \tag{59}$$

and

$$B = 2b\dot{\beta}_1^2(\underline{\varepsilon}\cdot\Delta\vec{n}) : (\underline{\varepsilon}\cdot\Delta\vec{n}). \tag{60}$$

Both A and B are scalar quantities. We see that

$$A\frac{1}{\sin^2\alpha} = B\frac{\cos\alpha}{\sin^3\alpha}, \tag{61}$$

and finally the expression for the angle α

$$\tan\alpha = \frac{B}{A} \text{ and } \alpha = \arctan\frac{B}{A}. \tag{62}$$

5. The optimal interacting fault system

In the previous chapter we derived equations relating the orientations of the intersecting faults and the rate-of-relative microrotation. From Eq. (46) it follows that there always exists interaction between equal sized intersecting faults producing parallel direction of slip. First, having the rate-of-deformation constant, the time can be eliminated from Eqs. (46) and (47), and the relative microrotation linearly depends on the instantaneous macrostrain:

$$\Delta\vec{s} = -\vec{\phi}^{\mathrm{rel}}\times\Delta\vec{n},$$
$$\left(\underline{\mathbf{T}}_1 - \frac{L_2}{L_1}\underline{\mathbf{T}}_2\right) : \mathbf{u}^{(S)} = -\vec{\phi}^{\mathrm{rel}}\times\left(\vec{n}_1 - \frac{L_2}{L_1}\vec{n}_2\right). \tag{63}$$

Assuming (1) the distances between adjacent block centroids measured perpendicular to the fault planes are equal, $L_i = L_j\ \forall_{i,j}$, and (2) the interacting faults of the interacting subsystem are characterized by the vector $\Delta\vec{n} = \vec{n}_i - \vec{n}_j$ subparallel to the relative microrotation vector $\vec{\phi}^{\mathrm{rel}}$, it follows from Eq. (63), $\Delta\vec{s} = -\vec{\phi}^{\mathrm{rel}}\times\Delta\vec{n}$, that the difference between the slip direction along the two intersecting faults, $\Delta\vec{s}$, is equal to 0. Because this difference does not depend on the magnitude of the relative microrotation, the slip direction along the pair of faults is parallel. We will call such a fault system "*the optimal interacting fault system*". Along the faults of this fault system the components of slip and shear stress due to the relative microrotation, $\gamma^c\vec{c} = L\underline{\mathbf{T}}:\mathbf{A}$ and $b\underline{\mathbf{T}}:\mathbf{A}$, have the same orientations as the vectors $\vec{d}$ and $\gamma^s\vec{s} = L\underline{\mathbf{T}}:\mathbf{u}^{(S)}$, while the actual direction can be the same or opposite, depending on the relative microrotation vector $\vec{\phi}^{\mathrm{rel}}$.

Eq. (63) also shows that the interaction in the optimal interacting system is only possible between two equal sized faults lying symmetrically with respect to the kinematic axes of the Cosserat strain tensor. Only for such pairs of faults the vector $\Delta\vec{n} = \vec{n}_i - \vec{n}_j$ is parallel to the relative microrotation vector $\vec{\phi}^{\mathrm{rel}}$. For other interacting pairs of equal sized faults $\Delta\vec{s}$ is not equal to 0, because the vector $\Delta\vec{n} = \vec{n}_i - \vec{n}_j$ is not parallel to the relative microrotation vector $\vec{\phi}^{\mathrm{rel}}$. When for the two non-optimal interacting equal sized faults the vector $\Delta\vec{s}$ is also equal to 0, they are related to zero relative microrotations $\vec{\phi}^{\mathrm{rel}} = 0$, because in this case $\Delta\vec{s} = -\vec{\phi}^{\mathrm{rel}}\times\Delta\vec{n} = 0$.

5.1. Dependence of the geometry of the optimal interacting system on the instantaneous deformation parameter D

We showed that the orientation of slip along the faults of the optimal interacting fault system does not depend on the relative microrotation. Both vectors, $\gamma^s\vec{s} = L\underline{\mathbf{T}}:\mathbf{u}^{(S)}$ and $\gamma^c\vec{c} = L\underline{\mathbf{T}}:\mathbf{A}$ are parallel. They have the same orientations while their actual direction can be the same or opposite, depending on the relative microrotation vector $\vec{\phi}^{\mathrm{rel}}$. However, the geometry of the optimal interacting system does depend on the orientations of the kinematic axes of the instantaneous macrostrain tensor $\mathbf{u}^{(S)}$ and on the instantaneous deformation parameter D, because the orientation of slip is defined by $\gamma^s\vec{s} = L\underline{\mathbf{T}}:\mathbf{u}^{(S)}$.

We will search for the exact analytical solutions for the geometry of the optimal interacting system depending on the parameter D in the classical continuum with no relative microrotation. The orientations of the kinematic axes will be constant (Fig. 2b). If the first fault of the optimal interacting system has the unit normal $\vec{n}_1 = (n_1, n_2, n_3)$, then the second fault has the unit normal (Fig. 2b) $\vec{n}_2 = (n_1, -n_2, n_3)$. The direction of slip along any fault is

$$\gamma^s\vec{s} = L\underline{\mathbf{T}}:\mathbf{u}^{(S)} = L\left(\mathbf{u}^{(S)}\vec{n} - \left(\mathbf{u}^{(S)}\vec{n}\cdot\vec{n}\right)\vec{n}\right). \tag{64}$$

Multiplication of the macrostrain tensor $\mathbf{u}^{(S)}$ by some scalar constant α and the addition of any component of volumetric strain $\beta\mathbf{1}$ do not affect the direction of slip

$$\gamma^s \vec{s}' = L\underline{\mathbf{T}} : \left(\alpha \mathbf{u}^{(S)} + \beta \mathbf{1}\right) = L\alpha \underline{\mathbf{T}} : \mathbf{u}^{(S)} + L\beta \underline{\mathbf{T}} : \mathbf{1} = L\alpha \underline{\mathbf{T}} : \mathbf{u}^{(S)} = \alpha \gamma_i^s \vec{s}, \tag{65}$$

because $L\beta \underline{\mathbf{T}} : \mathbf{1} = 0$. In the following calculation we will use the macrostrain tensor $\mathbf{u}^{(S)}$ of the form

$$\mathbf{u}^{(S)} = \begin{bmatrix} 1 & 0 & 0 \\ 0 & D & 0 \\ 0 & 0 & 0 \end{bmatrix}. \tag{66}$$

In the description of geologic faulting, this form of $\mathbf{u}^{(S)}$ has no physical sense, because in most cases the volume changes can be neglected, $\mathrm{Tr}(\mathbf{u}^{(S)}) = \lambda_1 + \lambda_2 + \lambda_3 = 0$. However, the above form of $\mathbf{u}^{(S)}$ does not affect the final results for the possible orientation of the optimal interacting system. For the slip $\gamma_1^s \vec{s}'_1$ along the first fault we have

$$\gamma_1^s \vec{s}'_1 = \begin{pmatrix} n_1 - (n_1^2 + Dn_2^2)n_1 \\ Dn_2 - (n_1^2 + Dn_2^2)n_2 \\ -(n_1^2 + Dn_2^2)n_3 \end{pmatrix}, \tag{67}$$

and for the second fault

$$\gamma_2^s \vec{s}'_2 = \begin{pmatrix} n_1 - (n_1^2 + Dn_2^2)n_1 \\ -Dn_2 + (n_1^2 + Dn_2^2)n_2 \\ -(n_1^2 + Dn_2^2)n_3 \end{pmatrix}. \tag{68}$$

Because the slip direction along both faults is equal and parallel to the intersection vector $\vec{d}$, we have

$$\gamma_1^s \vec{s}'_1 = \gamma_2^s \vec{s}'_2. \tag{69}$$

The first and the third components are always equal for both faults, because they do not depend on the sign of the component n_2. For the second component of the vectors $\gamma_1^s \vec{s}'_1$ and $\gamma_2^s \vec{s}'_2$, however, we can only have (see also Fig. 2b)

$$Dn_2 - \left(n_1^2 + Dn_2^2\right)n_2 = 0. \tag{70}$$

The components of the unit normals $\vec{n}_1$ and $\vec{n}_2$ can be expressed in terms of the second component n_2 of the vector $\vec{n}_1$. From Eq. (70) we have

$$n_1 = \sqrt{D(1 - n_2^2)}. \tag{71}$$

Taking into account that $\|\vec{n}_1\|^2 = n_1^2 + n_2^2 + n_3^2 = 1$, we can express vectors $\vec{n}_1$ and $\vec{n}_2$ in the following form:

$$\vec{n}_1 = \begin{pmatrix} \pm\sqrt{D(1 - n_2^2)} \\ n_2 \\ -\sqrt{(1 - D)(1 - n_2^2)} \end{pmatrix}, \tag{72}$$

$$\vec{n}_2 = \begin{pmatrix} \pm\sqrt{D(1 - n_2^2)} \\ -n_2 \\ -\sqrt{(1 - D)(1 - n_2^2)} \end{pmatrix}. \tag{73}$$

We always take the third component negative, so that the unit normal is directed downwards. In this case we have four possible solutions aligned symmetrically with respect to the kinematic axes of the macrostrain tensor $\mathbf{u}^{(S)}$ (Fig. 3). These four solutions form two *optimal subsystems of interacting faults*, the first dipping northwards and the second dipping southwards (Fig. 3). According to Eq. (42), the both interacting subsystems are characterized by intersection vectors $\vec{d}_1$ or $\vec{d}_2$

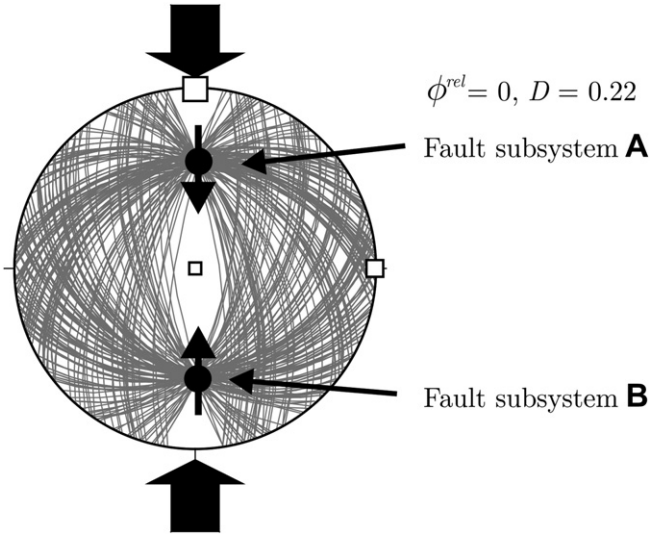

Fig. 3. Geometry of the optimal interacting system of faults in the classical (Cauchy) continuum. The total interacting system consists of two subsystems (Fault subsystems A and B) symmetrically aligned with respect to the kinematic axes of the instantaneous deformation tensor $\mathbf{u}^{(S)}$.

$$\vec{d}_1 = \left(\sqrt{1 - D}, 0, -\sqrt{D}\right)^T, \quad \vec{d}_2 = \left(-\sqrt{1 - D}, 0, -\sqrt{D}\right)^T. \tag{74}$$

The dip of the intersection vector is then

$$\delta = \arctan\sqrt{\frac{D}{1 - D}}. \tag{75}$$

For $D = 0$, the dip δ is equal to zero. For $D = 1$, the dip is 90°. For $0 < D < 1$, the dip is $0° < \delta < 90°$ (Fig. 4).

The value of the component n_2 in the above equations can be arbitrary chosen, therefore all faults with the unit normal $\vec{n}$ perpendicular to the intersection vectors $\vec{d}_1$ or $\vec{d}_2$ belong to the optimal intersection system. However, only pairs of faults with $\Delta\vec{n} = \vec{n}_i - \vec{n}_j$ parallel to the relative microrotation vector $\vec{\phi}^{\mathrm{rel}}$ can interact. We will define the *optimal plane*, which has the unit normal $\vec{d}_i$ (Fig. 2b).

Fig. 4 shows the geometry of the optimal interacting fault system for three different values of the parameter D; $D = 0$, $D = 0.22$ and $D = 1$. The intersection vectors $\vec{d}_1$ and $\vec{d}_2$ become subvertical as the parameter D increases toward 1. The cases of $D = 0$ and $D = 1$ are mathematically possible but physically have no sense, because the shear stress along the faults is equal to zero. For $D = 0$ we have $\lambda_2 = \lambda_3 = \lambda$ and the predicted faults of the optimal interacting fault system have the unit normals $\vec{n}_i$ in the plane defined by the vectors $\vec{\lambda}_2$ and $\vec{\lambda}_3$ (see Fig. 4). So $\vec{n}_i = \alpha\vec{\lambda}_2 + \beta\vec{\lambda}_3$, where α and β are some scalar parameters. This means that the vector $\vec{n}_i$ is the eigenvector of the symmetric part of the strain tensor, $\mathbf{u}^{(S)}$. Because of the linear constitutive equation between the stress and the strain, $\boldsymbol{\sigma} = p_r\mathbf{1} + a\mathbf{u}^{(S)}$ (see Eqs. (30) or (35)), the vector $\vec{n}_i$ is also the eigenvector of the stress tensor

$$\boldsymbol{\sigma}\vec{n}_i = \left(p_r\mathbf{1} + a\mathbf{u}^{(S)}\right)\cdot\left(\alpha\vec{\lambda}_2 + \beta\vec{\lambda}_3\right) = (p_r + a\lambda)\vec{n}_i = \sigma\vec{n}_i \tag{76}$$

The shear stress is then

$$\vec{\tau}_i = \underline{\mathbf{T}}_i : \boldsymbol{\sigma} = \boldsymbol{\sigma}\vec{n}_i - (\boldsymbol{\sigma}\vec{n}_i\cdot\vec{n}_i)\vec{n}_i = \sigma\vec{n}_i - \sigma\vec{n}_i = 0 \tag{77}$$

Similar calculation is also possible for the case $D = 1$.

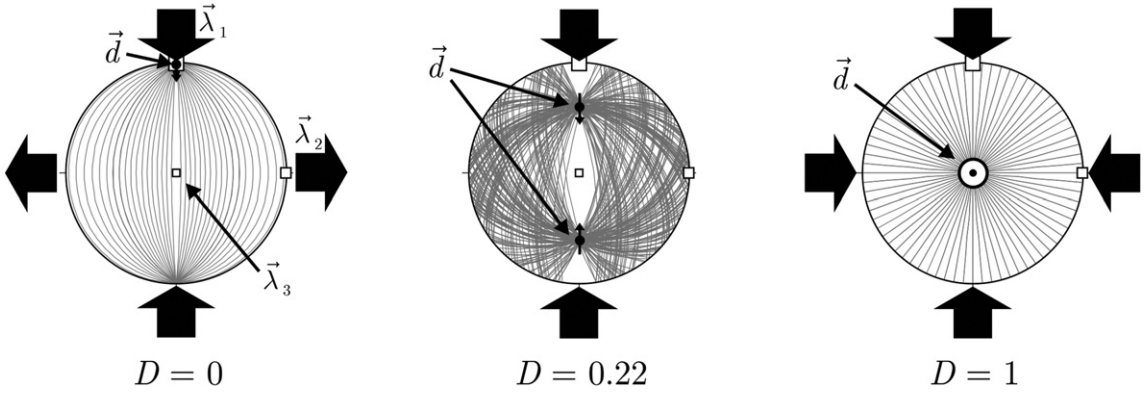

Fig. 4. Dependence of the geometry of the optimal interacting system on the instantaneous deformation parameter D for three different values of this parameter; $D = 0$, $D = 0.22$ and $D = 1$. For $D = 0$, the intersection vector $\vec{d}$ for all faults is horizontal, whilst for $D = 1$ the intersection vector $\vec{d}$ is vertical and points upwards (indicated by $\odot$). Both solutions are mathematically possible but physically have no sense, because the shear stress along the faults is equal to zero. For $0 < D < 1$, the total interacting system consists of two interacting subsystems. The value of the parameter D defines the dip of the intersection vector $\vec{d}$ for the both interacting fault subsystems. The larger the D, the larger the dip of the intersection vector $\vec{d}$.

5.2. Dependence of the geometry of the optimal interacting system on the relative microrotation

Based on the above discussion, the orientation of slip along the faults of the optimal interacting system does not depend on the relative microrotation but remains parallel to the intersection vector $\vec{d}_i$. However, we can show that the geometry of this system does depend (1) on the constitutive parameter b, (2) on the coefficient of friction $\mu = \tan\phi$ (ϕ is angle of friction), and (3) on the relative microrotation $\vec{\phi}^{\,\mathrm{rel}}$. First, it is important to have in mind that based on the proposed constitutive equation (Eq. (35)) the skew-symmetric component of stress tensor only affects the magnitude of shear stress (Žalohar and Vrabec, 2010). Since $\mathbf{A}\vec{n} = \vec{\phi}^{\,\mathrm{rel}} \times \vec{n}$, the stress on the fault is

$$\boldsymbol{\sigma}\vec{n} = p_r\vec{n} + a\mathbf{u}^{(\mathrm{S})}\vec{n} + b\mathbf{A}\vec{n} = p_r\vec{n} + a\mathbf{u}^{(\mathrm{S})}\vec{n} + b\vec{\phi}^{\,\mathrm{rel}} \times \vec{n}. \tag{78}$$

The vector $\mathbf{A}\vec{n} = \vec{\phi}^{\,\mathrm{rel}} \times \vec{n}$ is perpendicular to the unit normal $\vec{n}$ and, consequently, the contribution of the skew-symmetric component of the stress tensor lies in the fault plane. Changing the relative microrotation will therefore only affect the shear stress along the faults of the optimal interacting system.

Because the vectors $\gamma^s\vec{s} = L\underline{\mathbf{T}} : \mathbf{u}^{(\mathrm{S})}$ and $\gamma^c\vec{c} = L\underline{\mathbf{T}} : \mathbf{A}$ are both parallel to the intersection vector $\vec{d}_i$, the shear stress component due to the skew-symmetric component of stress $b\underline{\mathbf{T}} : \mathbf{A} = b\mathbf{A}\vec{n} = b\vec{\phi}^{\,\mathrm{rel}} \times \vec{n}$ is also parallel to the intersection vector $\vec{d}_i$. The vectors $\gamma^s\vec{s} = L\underline{\mathbf{T}} : \mathbf{u}^{(\mathrm{S})}$ and $\vec{d}_i$ have the same direction, while the vectors $\gamma^c\vec{c} = L\underline{\mathbf{T}} : \mathbf{A}$ and $b\underline{\mathbf{T}} : \mathbf{A}$ can have the same or the opposite direction (relative to the first two vectors), depending on the relative microrotation vector $\vec{\phi}^{\,\mathrm{rel}}$. Changing the magnitude of the relative microrotation will therefore affect the driving shear stress along the faults.

The Amontons' condition for slip along the director $\vec{d}_i$ is

$$\tau^r = \vec{\tau}\cdot\vec{d}_i \geq \mu\sigma_n, \tag{79}$$

or

$$\left(a\underline{\mathbf{T}} : \mathbf{u}^{(\mathrm{S})} + b\underline{\mathbf{T}} : \mathbf{A}\right)\cdot\vec{d}_i = \mu\left(p_r\mathbf{N} : 1 + a\mathbf{N} : \mathbf{u}^{(\mathrm{S})}\right), \tag{80}$$

or also

$$\left(p_r\vec{n} + a\mathbf{u}^{(\mathrm{S})}\vec{n} + b\vec{\phi}^{\,\mathrm{rel}} \times \vec{n}\right)\cdot\vec{d}_i \geq \mu\left(p_r\vec{n} + a\mathbf{u}^{(\mathrm{S})}\vec{n}\right)\cdot\vec{n}. \tag{81}$$

Note that the normal stress is $\sigma_n = \boldsymbol{\sigma}\vec{n}\cdot\vec{n}$ and the shear stress along the director $\vec{d}_i$ is $\tau^r = \boldsymbol{\sigma}\vec{n}\cdot\vec{d}_i$. Because $p_r\vec{n}\cdot\vec{d}_i = 0$, $(\vec{\phi}^{\,\mathrm{rel}} \times \vec{n})\cdot\vec{n} = 0$, $\vec{n}\cdot\vec{n} = 1$ and $\vec{\phi}^{\,\mathrm{rel}} = \phi^{\mathrm{rel}}\vec{\lambda}_2$ we may write

$$a\mathbf{u}^{(\mathrm{S})}\vec{n}\cdot\vec{d}_i + b\phi^{\mathrm{rel}}(\vec{\lambda}_2 \times \vec{n})\cdot\vec{d}_i \geq \mu\left(p_r + a\mathbf{u}^{(\mathrm{S})}\vec{n}\cdot\vec{n}\right). \tag{82}$$

From here we can express ϕ^{rel}. For the northward dipping faults on Fig. 3 the term $b(\vec{\lambda}_2 \times \vec{n})\cdot\vec{d}_i$ is negative, therefore

$$\phi^{\mathrm{rel}} \leq \frac{\mu\left(p_r + a\mathbf{u}^{(\mathrm{S})}\vec{n}\cdot\vec{n}\right) - a\mathbf{u}^{(\mathrm{S})}\vec{n}\cdot\vec{d}_i}{b(\vec{\lambda}_2 \times \vec{n})\cdot\vec{d}_i} = \frac{|\tau^{(\mathrm{S})} - \mu\sigma_n|}{|b(\vec{\lambda}_2 \times \vec{n})\cdot\vec{d}_i|} = \phi_0^{\mathrm{rel}}, \tag{83}$$

with $\tau^{(\mathrm{S})} = a\mathbf{u}^{(\mathrm{S})}\vec{n}\cdot\vec{d}_i$ being the shear stress component along the director $\vec{d}_i$ related to the symmetric part of the stress tensor. For negative values of the relative microrotation ϕ^{rel}, the shear stress along these faults is larger and *vice versa*. The maximum physically reasonable value of the ϕ_0^{rel} according to Eq. (5) is $\phi_{\max}^{\mathrm{rel}} = 0.5(\lambda_1 - \lambda_3)$. For southward dipping faults on Fig. 3 the term $b(\vec{\lambda}_2 \times \vec{n})\cdot\vec{d}_i$ is positive, therefore

$$\phi^{\mathrm{rel}} \geq \frac{\mu\left(p_r + a\mathbf{u}^{(\mathrm{S})}\vec{n}\cdot\vec{n}\right) - a\mathbf{u}^{(\mathrm{S})}\vec{n}\cdot\vec{d}_i}{b(\vec{\lambda}_2 \times \vec{n})\cdot\vec{d}_i} = -\frac{|\tau^{(\mathrm{S})} - \mu\sigma_n|}{|b(\vec{\lambda}_2 \times \vec{n})\cdot\vec{d}_i|} = -\phi_0^{\mathrm{rel}}. \tag{84}$$

For positive values of the relative microrotation ϕ^{rel}, the shear stress along these faults is larger and *vice versa*. Having the orientations of the kinematic axes as on Figs. 2 and 3, the northward dipping faults can only be active if the relative microrotation ϕ^{rel} has some value that is smaller than ϕ_0^{rel}, whilst the southward dipping faults can be active when the relative microrotation ϕ^{rel} has value larger than $-\phi_0^{\mathrm{rel}}$. The total optimal interacting system of faults in the Cosserat continuum is thus asymmetrical (Fig. 5). We can have the following situations (see also Fig. 5):

1. $\phi_0^{\mathrm{rel}} \neq 0$, $-\phi_0^{\mathrm{rel}} \leq \phi^{\mathrm{rel}} \leq \phi_0^{\mathrm{rel}}$ (Fig. 5a and c). The slip is possible on both optimal interacting subsystems of faults. However, one subsystem is dominant over the other, depending on the sign of ϕ^{rel}. For example, if we take ϕ^{rel} negative, the shear stress along the northward dipping faults (Fig. 3a) will be higher as along the southward dipping faults. Therefore, the northward dipping optimal interacting subsystem will be the dominant.

2. $\phi_0^{\mathrm{rel}} \neq 0, \phi^{\mathrm{rel}} < -\phi_0^{\mathrm{rel}}$ *or* $\phi^{\mathrm{rel}} > \phi_0^{\mathrm{rel}}$ (Fig. 5b and d). The slip is possible only on a single optimal interacting subsystem of faults, depending on the sign of ϕ^{rel}. For $\phi^{\mathrm{rel}} > \phi_0^{\mathrm{rel}}$ the slip is only possible on the southward dipping faults. For $\phi^{\mathrm{rel}} < -\phi_0^{\mathrm{rel}}$ the slip is only possible on the northward dipping faults.

Fig. 5 illustrates the geometry of the optimal interacting fault system in the Cosserat continuum for the value of the instantaneous deformation parameter $D = 0.22$. For other values of the parameter D, where $0 < D < 1$, the geometry of the optimal interacting fault system is also similar. Varying the value of D only affects the dip of the intersection vectors $\vec{d}_1$ and/or $\vec{d}_2$ according to Eq. (75).

6. The non-optimal interacting systems

A chosen non-optimally orientated fault has the unit normal $\vec{n}$ that is not perpendicular to neither of the vectors $\vec{d}_1$ nor $\vec{d}_2$. In the coordinate system defined by the base vectors $\vec{\lambda}_2$, $\vec{d}_i$ and $\vec{n}_0 = \vec{\lambda}_2 \times \vec{d}_i$ the vector normal $\vec{n}$ can be written as

$$\vec{n} = \alpha \vec{\lambda}_2 + \beta \vec{n}_0 + \gamma \vec{d}_i \tag{85}$$

The contribution of the relative microrotation to the slip direction is

$$L\underline{\mathbf{T}} : \mathbf{A} = L\vec{\phi}^{\mathrm{rel}} \times \vec{n} = L\alpha \vec{\phi}^{\mathrm{rel}} \times \vec{\lambda}_2 + L\beta \vec{\phi}^{\mathrm{rel}} \times \vec{n}_0 + L\gamma \vec{\phi}^{\mathrm{rel}} \times \vec{d}_i \tag{86}$$

The first component is always equal to zero, $L\alpha \vec{\phi}^{\mathrm{rel}} \times \vec{\lambda}_2 = 0$, because $\vec{\phi}^{\mathrm{rel}}$ is parallel to the $\vec{\lambda}_2$. The second component is parallel to $\vec{d}_i$, while the third component is perpendicular to $\vec{d}_i$. We see that in the case when the component of the unit normal $\vec{n}$ along the base vector $\vec{n}_0 = \vec{\lambda}_2 \times \vec{d}_i$ is large, the contribution of the relative microrotation to the slip direction is parallel to the director of the optimal interacting subsystem $\vec{d}_i$.

The Amontons' condition for slip to be possible depends on the contribution of the relative microrotation to the shear stress, $b\underline{\mathbf{T}} : \mathbf{A}$. It is important to have in mind that the component of slip due to the macrostrain, $\gamma^s \vec{s} = L\underline{\mathbf{T}} : \mathbf{u}^{(S)}$, and the shear stress component due to the symmetric part of the stress tensor, $a\underline{\mathbf{T}} : \mathbf{u}^{(S)}$, are both parallel. The contribution of the relative microrotation to the slip direction, $\gamma^c \vec{c} = L\underline{\mathbf{T}} : \mathbf{A}$ is also parallel to the contribution of the relative microrotation to the shear stress, $b\underline{\mathbf{T}} : \mathbf{A}$. However, the resulting slip direction $\gamma \vec{m} = L\underline{\mathbf{T}} : \mathbf{u}^{(S)} + L\underline{\mathbf{T}} : \mathbf{A}$ is not parallel to the resulting shear stress $\vec{\tau} = \underline{\mathbf{T}} : \boldsymbol{\sigma} = a\underline{\mathbf{T}} : \mathbf{u}^{(S)} + b\underline{\mathbf{T}} : \mathbf{A}$, at least when $a \neq b$. Although the direction of slip along some non-optimal faults

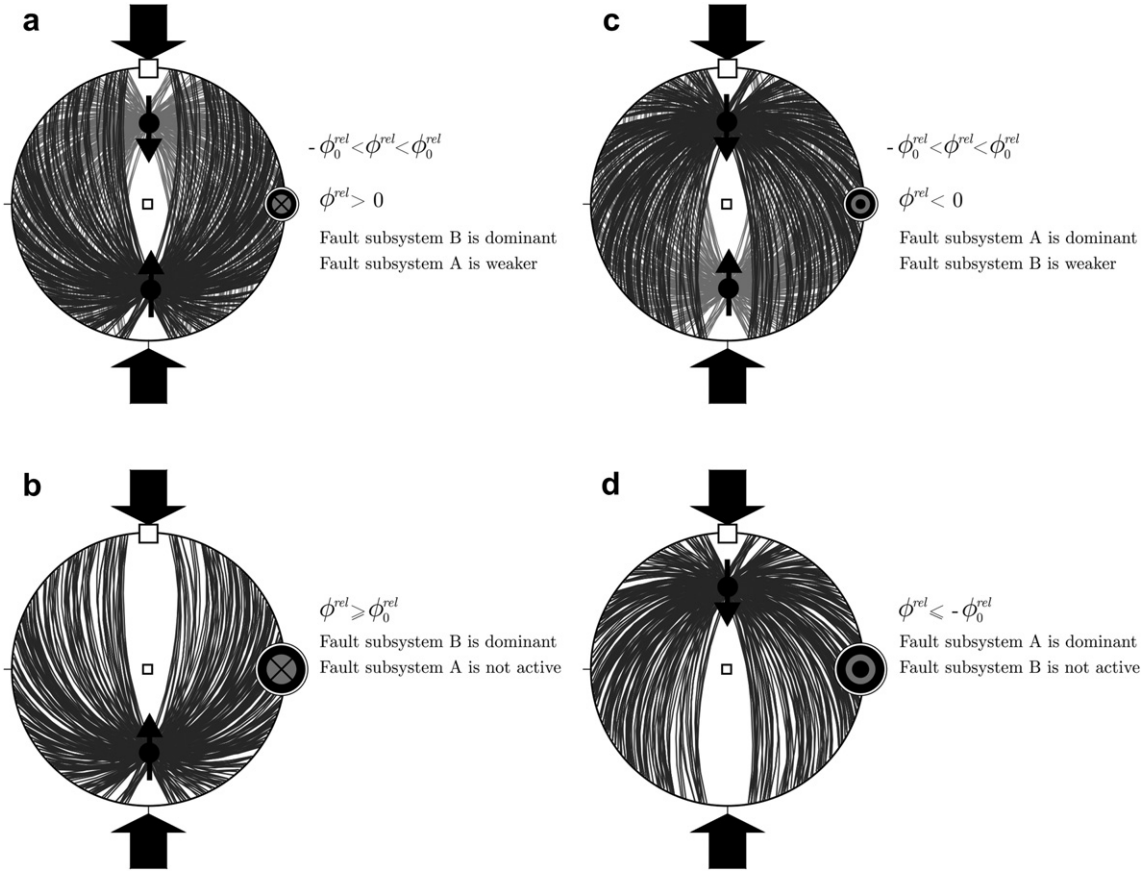

Fig. 5. Geometry of the optimal interacting system depending on the relative microrotation ϕ^{rel}. In all cases the value of the instantaneous deformation parameter was $D = 0.22$. In the Cosserat continuum the optimal interacting subsystems are not symmetrical, because the shear and the shear stress along the faults of the two optimal interacting subsystems do not have the same magnitude. Depending (1) on the orientations of the kinematic axes of the instantaneous strain tensor $\mathbf{u}^{(S)}$, (2) on the sign of the relative microrotation, and (3) on the properties of the constitutive equation relating the stress and the strain, one of the interacting subsystems becomes dominant, while the other becomes weaker (cases (a) and (c)). The dominant subsystem accommodates a larger amount of deformation, because the resolved shear and shear stress along the faults of this subsystem are higher. For large relative microrotation, the faults of the weaker subsystem are impossible to slip, and the total optimal interacting system consists of a single subsystem (cases (b) and (d)). See text for details.

might be subparallel to the intersection vector $\vec{d}_i$, some orientations of these faults are unsuitable for slip to be possible. We can expect that the geometry of the non-optimal interacting system depends (1) on the friction coefficient μ and (2) on the asymmetry of the stress defined by the constitutive parameter b and relative microrotation $\vec{\phi}^{\text{rel}}$. Theoretically, we have the following situations:

1. For all faults with orientations close to the dominant optimal interacting subsystem the components $\gamma^c\vec{c} = L\underline{\mathbf{T}} : \mathbf{A}$ (=contribution of the relative microrotation to the slip direction) and $b\underline{\mathbf{T}} : \mathbf{A}$ (=contribution of the relative microrotation to the shear stress) are approximately in the same direction as the corresponding vectors $\gamma^s\vec{s} = L\underline{\mathbf{T}} : \mathbf{u}^{(S)}, a\underline{\mathbf{T}} : \mathbf{u}^{(S)}$, and $\vec{d}_i$ for that subsystem. The slip direction along these faults becomes subparallel to the vector $\vec{d}_i$ as the relative microrotation increases (Fig. 6a). The driving shear stress increases and the faults are highly possible to slip.
2. Contrary, for all faults with orientations close to the weaker (inferior) optimal interacting subsystem, the both components $\gamma^c\vec{c} = L\underline{\mathbf{T}} : \mathbf{A}$ and $b\underline{\mathbf{T}} : \mathbf{A}$ are approximately in the opposite direction as the vectors $\gamma^s\vec{s} = L\underline{\mathbf{T}} : \mathbf{u}^{(S)}, a\underline{\mathbf{T}} : \mathbf{u}^{(S)}$ and $\vec{d}_i$ for that subsystem. The magnitude of the shear stress along these faults decreases when the relative microrotation increases. Therefore, the slip along the faults is becoming less probable and the slip direction does not become subparallel to the intersection vector $\vec{d}_i$ of the weaker optimal interacting subsystem (Fig. 6b).

We may suppose that the Amontons' condition for a slip is fulfilled for non-optimal faults with orientations close to the dominant optimal interacting subsystem. These faults will probably interact (1) each other and (2) with faults of the dominant optimal interacting subsystem. This hypothesis is further discussed in the following chapters.

7. Numerical tests

The theory presented in the previous chapters was tested performing several numerical tests using the AmontonsWin computer program, which is part of the T-TECTO software. AmontonsWin generates a prescribed number of faults, which are either randomly orientated or follow a pre-defined distribution of orientations. The direction of slip along the faults is then set parallel to the resolved shear direction on the fault planes, calculated from the input Cosserat strain tensor according to the equation $\gamma\vec{m} = L\underline{\mathbf{T}} : \mathbf{e}$. The faults can only be activated when the resolved remote shear stress in the direction of slip exceeds the frictional resistance for sliding according to Amontons' law, Eq. (41). Even from the randomly generated population of faults, only the faults with mechanically suitable orientations are accepted by the AmontonsWin program, thus providing insights into possible geometries of slip-capable fault systems under various stress–strain boundary conditions. The aim of the tests described below was to analyze the effect of the relative microrotation on the geometry of interacting subsystems of faults having slip direction subparallel to the common intersection direction. In all tests it was assumed that the size of the faults is equal, which is an obvious simplification.

7.1. Test 1

In Test 1 we analyzed the effect of the relative microrotation on the direction of slip along the non-optimally orientated faults. In this test, 2000 faults with random distribution were generated setting the vorticity parameter to the value $C = -1$ and the constitutive parameter b to the value $b = 0.5$. The other constitutive parameters were $a = 1 - b = 0.5$, and $p_r = 0.22$. The coefficient of friction was $\mu = \tan 20^\circ$ and the instantaneous deformation parameter was $D = 0.22$. High absolute value of the vorticity parameter C was used because in this case the effect of the relative microrotation can be studied most easily. The value $b = 0.5$ was used to assure the parallelism between the shear stress and slip direction (Eq. (37)). Possible orientations of all slip-capable faults are shown in Fig. 7a by using the tangent-lineation plots.

In the next step, the number of pairs of intersecting faults was counted having the slip direction subparallel to the intersection vector (director) of the pair within the angular threshold of 20°. Each fault was associated by the index number N, which is the number of all other intersecting faults having subparallel direction of movement. In this test, the angle 20° refers to the threshold above which the slip directions are considered no longer subparallel to the intersection line for the two faults. The 20° value was used because in the stress–strain analysis of fault-slip data the natural dispersions often lead to distribution of angular misfits (for example between the theoretical and actual direction of slip) characterized by the standard deviation between 10° and 30° (Žalohar and Vrabec, 2007, 2008, 2010).

Fig. 7b shows tangent-lineation plots for 1272 faults that have the largest value of the index number, $N > 400$. Fig. 8 shows theoretical slip direction along these faults for five values of the vorticity parameter; $C = 1$, $C = 0.5$, $C = 0$, $C = -0.5$, and $C = -1$. When the vorticity parameter C goes toward -1, the slip direction along the faults with the unit normal approximately perpendicular to the

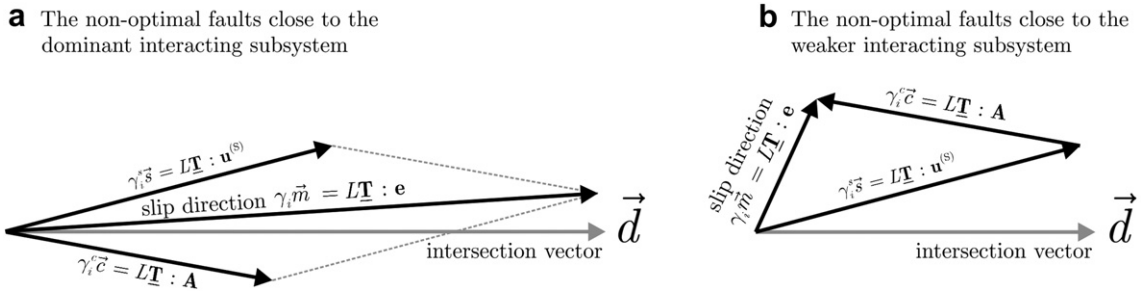

Fig. 6. Effect of the relative microrotation on the slip direction along the non-optimal faults. (a) Along the faults close to the dominant interacting subsystem the component of slip due to the instantaneous macrostrain $\gamma^s\vec{s} = L\underline{\mathbf{T}} : \mathbf{u}^{(S)}$ and the component of slip due to the relative microrotation $\gamma^c\vec{c} = L\underline{\mathbf{T}} : \mathbf{A}$ are both subparallel to the intersection vector $\vec{d}_i$ for the dominant interacting subsystem. Both components also have the same direction. Therefore, the slip direction along the faults will become subparallel to the intersection vector $\vec{d}_i$ as the relative microrotation increases. (b) Along the non-optimal faults close to the weaker interacting subsystem the vector $\gamma^c\vec{c} = L\underline{\mathbf{T}} : \mathbf{A}$ has approximately the opposite direction relative to the vector $\vec{d}_i$ for that subsystem. Therefore, the slip direction along the faults will not become subparallel to the intersection vector $\vec{d}_i$ as the relative microrotation increases.

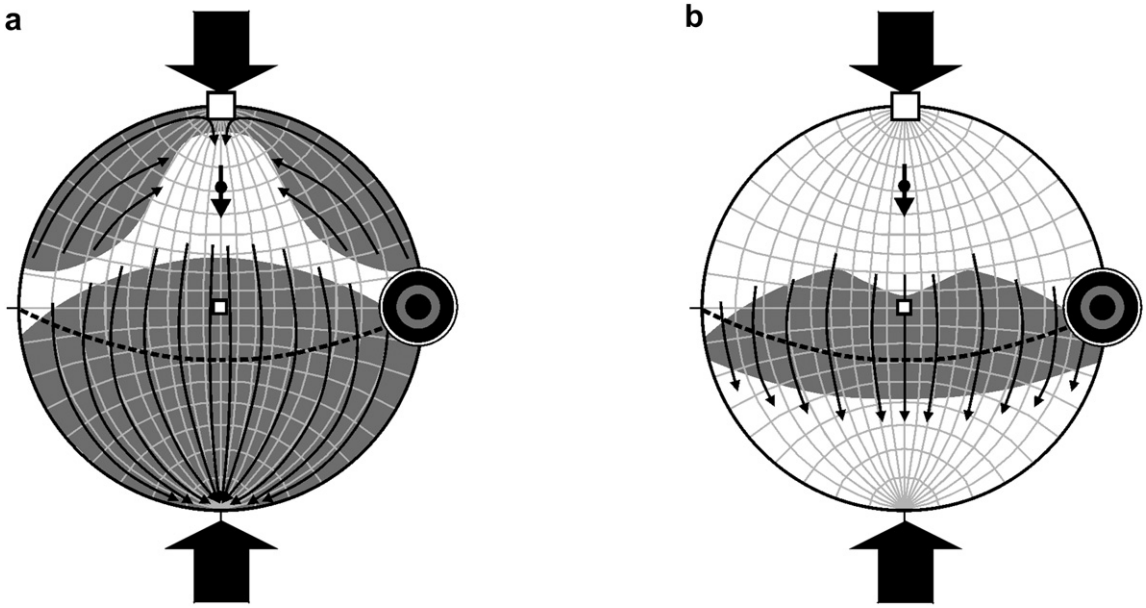

Fig. 7. Tangent-lineation diagrams for the results of Test 1. The possible orientations of the unit normals for the slip-capable faults are confined to the gray areas. The slip directions on the fault planes that are tangent to the plotting hemisphere at their slip plane poles are indicated by the field of arrows, which show the directions of slip of the material outside the plotting hemisphere (in general the footwall block) relative to the material within the hemisphere (the hangingwall block). (a) Tangent-lineation diagram for 2000 artificially generated faults in the Cosserat continuum with intensive relative microrotation ($C=-1$) and in an asymmetric stress field ($b=0.5$). (b) Tangent-lineation diagram for 1272 faults with the largest value of the index number, $N>400$. The index number defines the number of intersecting faults with subparallel direction of movement. This fault subsystem is highly asymmetric and the slip direction along all faults is subparallel within the angular threshold 20°. See text for details.

intersection vector $\vec{d}$ (belonging to the dominant slip-capable optimal interacting subsystem) becomes subparallel to the vector $\vec{d}$. We therefore suppose that many non-optimally orientated faults can also interact each other and with the faults of the dominant optimal interacting subsystem.

7.2. Test 2

The effect of the relative microrotation on the faults that are approximately perpendicular to the intersection vector $\vec{d}$ (belonging to the dominant optimal interacting subsystem) is further illustrated in Test 2. In this test, the effect of the relative microrotation on the slip direction was analyzed in the case of an interacting system consisting of two intersecting fault sets (Fig. 9). All faults in Fig. 9 were generated in the following manner. First, two optimal faults with the unit normals $\vec{n}_1$ and $\vec{n}_2$ belonging to the northward dipping dominant optimal interacting fault subsystem were selected in such a way that the difference $\Delta\vec{n} = \vec{n}_1 - \vec{n}_2$ was parallel to the relative microrotation $\vec{\phi}^{\,\mathrm{rel}}$ (and intermediate kinematic axis $\vec{\lambda}_2$). In the second step the faults of the both fault sets were generated by adding a random angular noise to orientations of the unit normals $\vec{n}_1$ and $\vec{n}_2$. The angular threshold of the noise was 10°. In this way, 20 fault planes were generated for each fault set. The state of stress and the direction of slip along the generated fault planes were then calculated by using the following values of the parameters $C=-1$, $a=0.5$, $b=0.5$, $p_r=0.22$, and $D=0.22$. The coefficient of friction was $\mu=\tan 20°$. In the next step, the value of the vorticity parameter C was varied from $+1$ to -1.

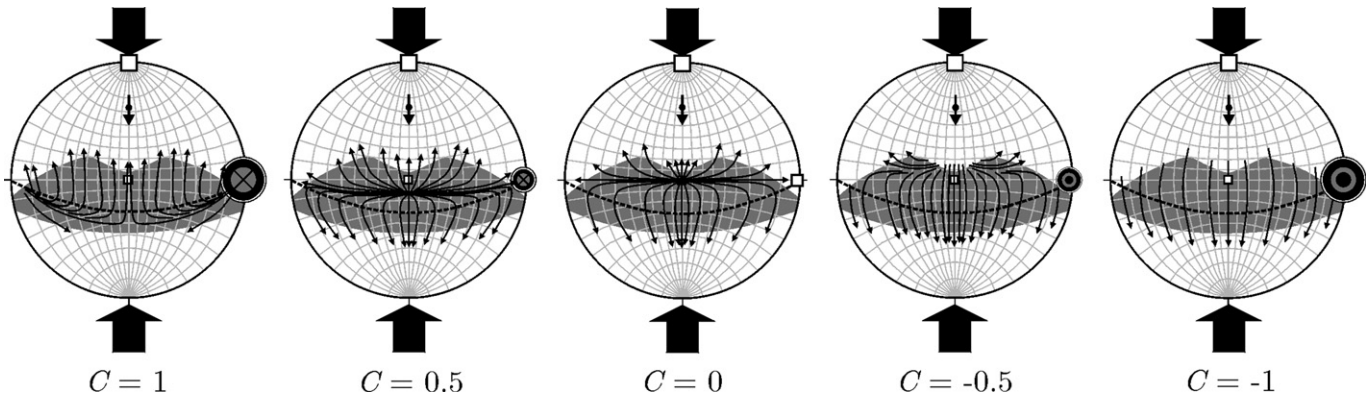

Fig. 8. Results of Test 1. Tangent-lineation diagram for 1272 faults with the largest index number, $N>400$. The possible orientation of the unit normal for the slip-capable faults is confined to the gray area. The field of arrows illustrates how the slip direction depends on the relative microrotation in the case of five possible values of the vorticity parameter; $C=1$, $C=0.5$, $C=0$, $C=-0.5$, and $C=-1$. The contra-clockwise direction of the relative microrotation around the $\vec{\lambda}_2$ axis is marked with ⊙, while the clockwise direction is marked with ⊗. When the vorticity parameter C goes toward -1, the slip direction along the faults with the unit normal close to the optimal plane (belonging to the dominant slip-capable optimal interacting subsystem) becomes subparallel to the common intersection of the dominant optimal interacting subsystem.

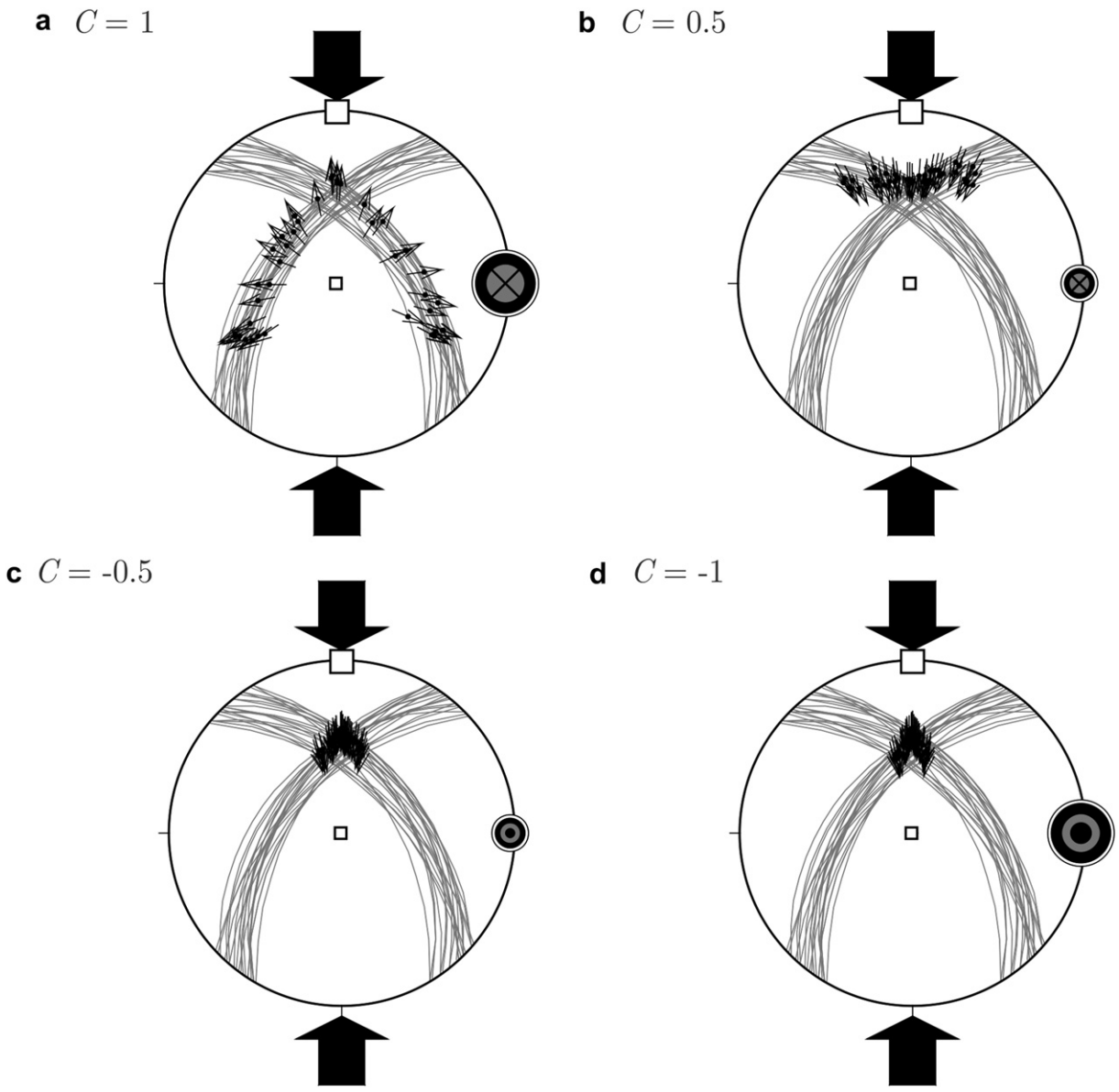

Fig. 9. Results of Test 2 analyzing the influence of the magnitude of the relative microrotation on the slip direction along two intersecting fault sets. The fault sets have optimal intersecting orientations for the vorticity parameter $C = -1$. Therefore, the slip direction along all faults concentrates around the common intersection direction when C goes toward -1. The contra-clockwise direction of the relative microrotation around the $\vec{\lambda}_2$ axis is marked with $\odot$, while the clockwise direction is marked with $\otimes$. See text for details.

Fig. 9 shows results of such tests for the following values of the vorticity parameter: $C = +1$, $C = +0.5$, $C = -0.5$ and $C = -1$. The slip direction along all faults concentrates around the common intersection direction when the vorticity parameter goes toward -1.

Test 2 additionally shows that the slip direction on the faults of the optimal interacting system is highly numerically unstable. Changing orientation of a chosen fault of the optimal interacting system for a small amount has a significant effect on the slip direction. Even if discrepancies from the optimal fault orientation are small, a high magnitude of the relative microrotation is needed in order the slip direction becomes parallel to the intersection line.

7.3. Test 3

In Test 3 we analyzed how the geometry of the interacting fault system depends on the constitutive parameter b and on the asymmetry of the stress tensor. We generated 2000 faults in three different stress and strain boundary conditions (Fig. 10). In the first case (Fig. 10a), the values of the constitutive parameters were $a = 0.3$, $b = 0.8$, and $p_r = 0.22$. In the second case (Fig. 10b), the values of the constitutive parameters were $a = 0.5$, $b = 0.5$, and $p_r = 0.22$. In the third case (Fig. 10c), however, we used the symmetric stress state defined by $a = 1$, $b = 0$, and $p_r = 0.22$. In both cases the instantaneous deformation parameter was $D = 0.22$ and the friction coefficient was relatively high, $\mu = \tan 50^\circ$. Again, we used a high absolute value of the relative microrotation parameter, $C = -1$, because in this case the effects of the relative microrotation can be studied most clearly. A high value of the friction coefficient was used to find the fault orientations characterized by the highest value of the driving shear stress.

Comparing to the results of Test 2 (compare Figs. 7a and 10b), it is clear that high value of the friction coefficient significantly reduces the subspace of the slip-capable fault orientations. It is also important that all slip-capable faults with orientations close to the

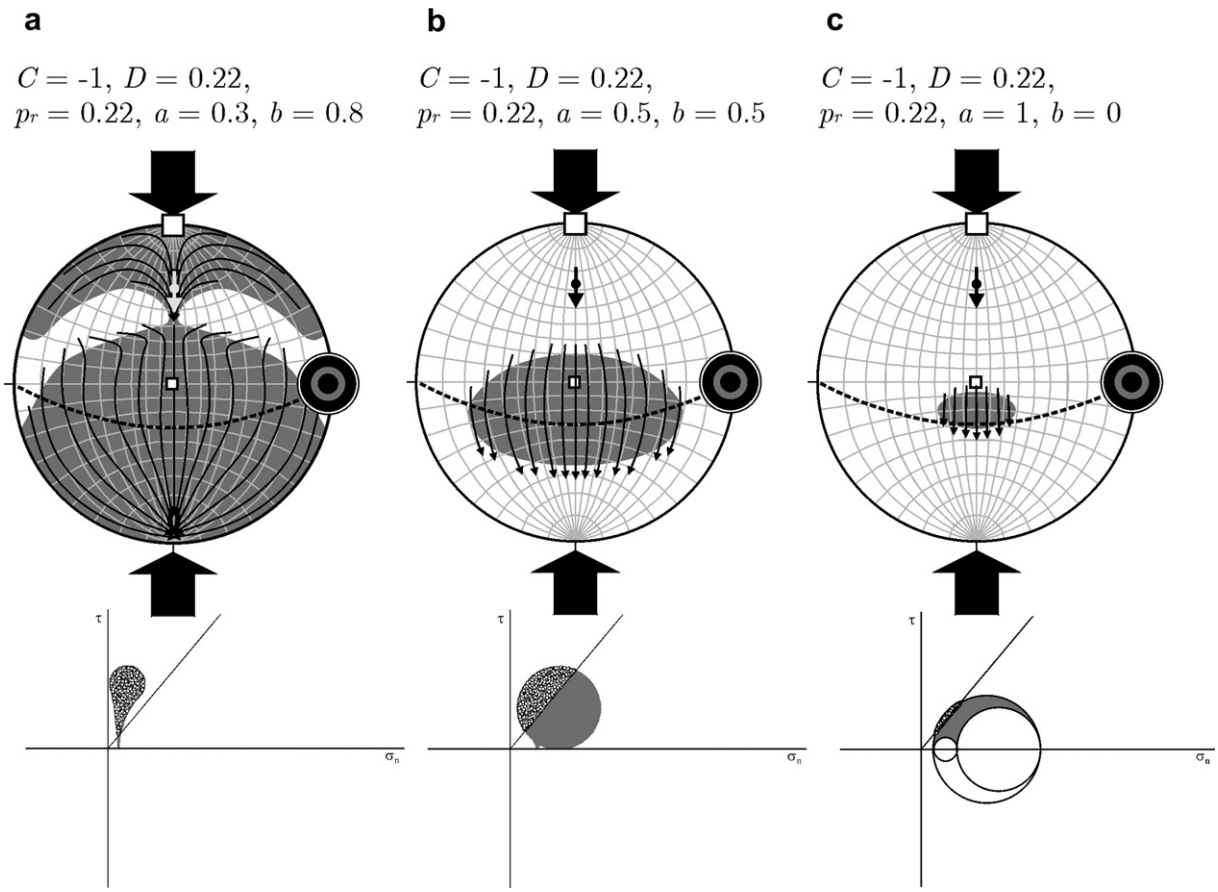

Fig. 10. Results of Test 3. Tangent-lineation diagram illustrating the possible orientations of the slip-capable faults depending on the asymmetry of the stress tensor. The possible orientation of the unit normal for the slip-capable faults is confined to the gray area and the slip direction along the faults is illustrated by the field of arrows. The state of stress on the faults is illustrated by the Mohr diagrams for the Cosserat continuum (see Žalohar and Vrabec, 2010). The increasing symmetry of the stress reduces the subspace of possible orientations of slip-capable faults, because the shear stress on most faults decreases. This subspace is the largest for highly asymmetric stress in the case (a) where the value of the constitutive parameter was $b = 0.8$. The subspace is smaller in the case (b) where the value of the constitutive parameter was $b = 0.5$. In the case (c) the symmetric stress was used, $b = 0$. Here, the slip-capable faults have the unit normal subparallel to the optimal plane belonging to the dominant interacting subsystem. See text for details.

optimal plane belonging to the dominant interacting subsystem have the slip direction subparallel to the intersection vector $\vec{d}$ (of the dominant interacting subsystem) and are therefore expected to interact with this subsystem. Based on the results of Test 3, the highest driving stress is found along the intersecting faults with the vector normal $\vec{n}$ subparallel to the vector $\vec{n}_0 = \vec{\lambda}_2 \times \vec{d}$. The driving shear stress along the faults of the weaker optimal interacting subsystem (and non-optimal faults close to it) is smaller or even negative. In the case of high relative microrotation and/or high friction coefficient these faults are very unlikely to slip (see Chapter 5).

The subspace of the possible fault orientation is further reduced by the symmetry of the stress tensor. For the symmetric stress tensor, the slip-capable fault orientations are limited to the highly confined subspace subparallel to the vector $\vec{n}_0 = \vec{\lambda}_2 \times \vec{d}$. In the case of the increasing asymmetry of the stress, $b \to 1$, this subspace becomes broader and numerous slip-capable fault planes are subparallel to the maximum kinematic axis $\vec{\lambda}_1$. The unit normals of these faults are subparallel to $\vec{\lambda}_3$.

7.4. Test 4

In this test, one natural fault system observed in the Povodje quarry in Slovenia was analyzed (Fig. 11). The studied area belongs to the Southern Alps folds-and-thrusts belt (Placer, 1999). In the Povodje quarry (longitude = 46°08′30″; latitude = 14°29′06″) numerous medium sized faults (with length less than 10 m) can be observed in the Upper Triassic limestone, which is thrust upon the Lower Permian clastic rocks (Premru, 1983a,b). The fault system consists of reverse faults, all having approximately equal dip but the dip direction is very dispersed. In addition, the direction of slip vectors on all faults is concentrated around the average common intersection among the faults. The fault system was analyzed by the T-TECTO computer program using the Cosserat inverse method described by Žalohar and Vrabec (2010). This method finds the Cosserat strain and corresponding stress tensors that describe best (1) the slip direction along the observed faults and (2) the geometry of the observed fault system. However, the method cannot automatically find the best values of the constitutive parameters a and b, and the friction coefficient μ. The value of these parameters should be set by the user. This means that many tests should be performed in order to find structurally acceptable results. For some optimal values of the constitutive parameters a and b, and the friction coefficient μ, the T-TECTO output includes (1) the orientations of the kinematic axes of the Cosserat strain tensor, $\vec{\lambda}_1$, $\vec{\lambda}_2$, $\vec{\lambda}_3$, (2) the relative values of the principal strains, λ_1, λ_2, λ_3, (3) the value of the instantaneous deformation parameter D, (4) the orientation of the relative microrotation vector, $\vec{\phi}^{\mathrm{rel}}$, (5) the value of the relative microrotation (or vorticity) parameter C, (6) the stress tensor $\boldsymbol{\sigma}$, and numerous other parameters that are helpful in structural interpretation of the observed fault system.

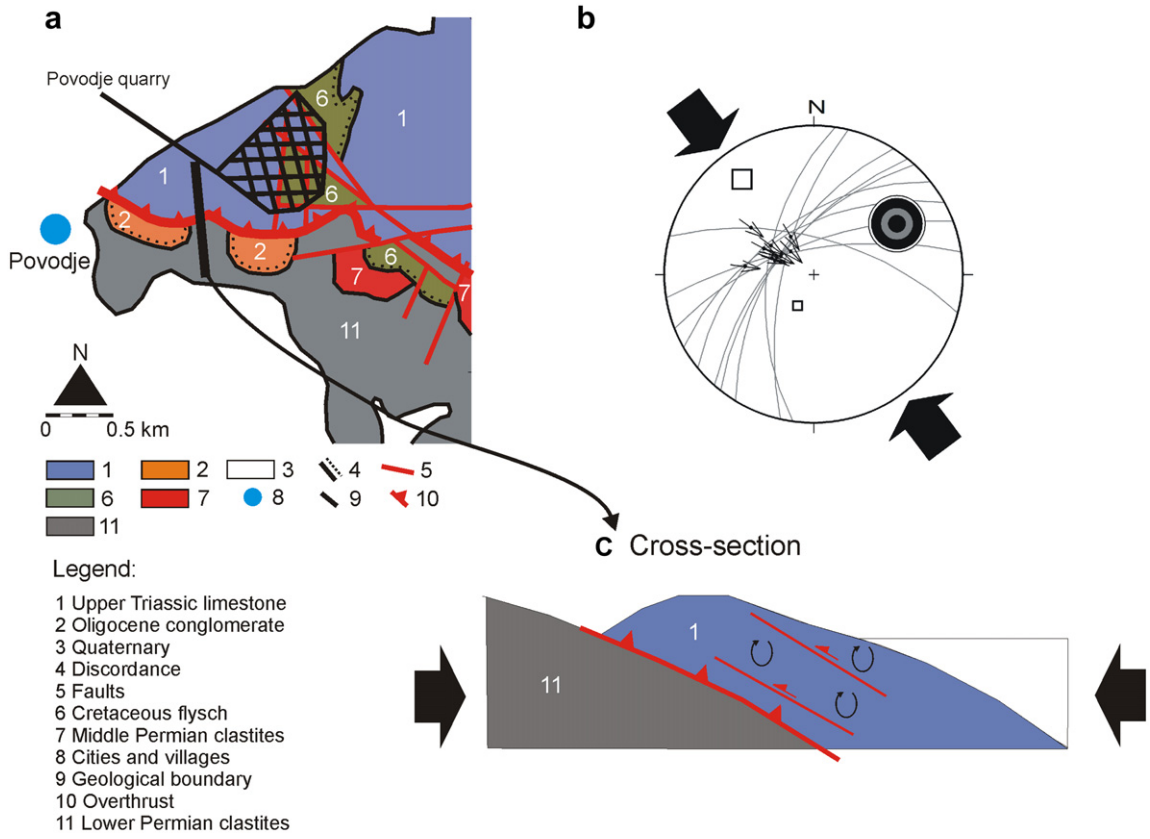

Fig. 11. Results of Test 4, where a natural fault system in the Povodje quarry (Slovenia) was analyzed. (a) Simplified geologic map of the area (Grad and Ferjančič, 1968; Premru, 1983a). (b) Results of the Cosserat inversion analysis (Žalohar and Vrabec, 2010) defining the best-fitting stress and strain tensors. The faults indicate NW-SE subhorizontal contraction and intensive relative microrotation in the contra-clockwise direction around the subhorizontal axis shown by ⊙. Faults have various orientations, however, the slip direction along all faults is concentrated around the average common intersection direction among the fault planes. Such fault system is characteristic for the wedge faulting in the Cosserat continuum. (c) Cross-section of the region. The Upper Triassic limestone is thrust over the Lower Permian clastic rocks. See text for details.

In Test 4, the inversion procedure was performed for all possible values of the constitutive parameter b (with $a = 1 - b$), ranging from zero to one with resolution of 0.1 (eleven tests). In all cases the results indicate intensive relative microrotations with $C = -1$. This means that the reactivation of the faults should be explained within the frame of the Cosserat theory. In addition, for all values of b the orientations of the calculated kinematic axes were stable and subparallel to orientations shown in Fig. 11. The approximate value of the constitutive parameter b can be found by comparing the geometry of the observed fault system to the theoretically generated fault system geometry (using the AmontonsWin computer program) in similar strain and stress boundary conditions. The results of two such tests are shown in Fig. 12. The geometry of the generated fault system was most similar to that actually observed in the quarry, when the following values of the constitutive parameters were used; $a = 1$, $b = 0$, $p_r = 0.49$, and $\mu \geq \tan 40^\circ$. The value of the parameter D only influences the dip of the common intersection vector, therefore we used the plane strain defined by $D = 0.5$.

Based on the results of Test 3, one of the criteria to recognize the symmetric or asymmetric stress states in the Earth's crust is the presence or absence of the fault planes that are subparallel to the maximum kinematic axis $\vec{\lambda}_1$. In the case of the Povodje fault

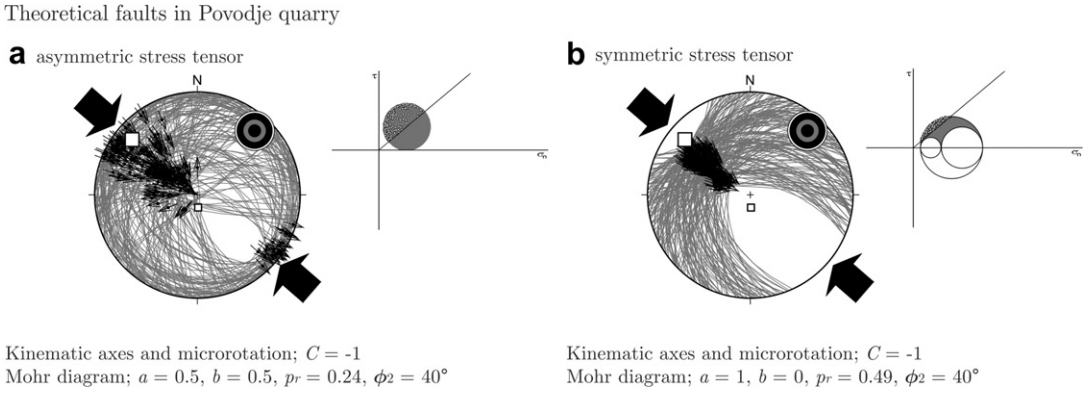

Fig. 12. Two artificial fault systems formed in the same strain boundary conditions as calculated in Fig. 11 analyzing the natural fault system in the Povodje quarry. (a) Asymmetric stress field with $b = 0.5$. (b) Symmetric stress field with $b = 0$. The most similar fault system geometry to that observed in nature is produced in the symmetric stress field. See text for details.

system, such fault planes are absent. This indicates the (almost) symmetric stress state defined by a small value of the constitutive parameter, $b \approx 0$.

Based on the above discussion, the value of the friction coefficient used in the inversion was $\mu = \tan 40^\circ$ and the value of the constitutive parameter b was equal to zero, $b = 0$. The results of the inversion procedure are shown in Fig. 11. They indicate NW-SE maximum contraction of the region, subvertical maximum extension of the rock massif, while in the direction of the intermediate kinematic axis of the instantaneous macrostrain tensor there is no deformation (plain strain, $D = 0.5$). Note that in the inversion procedure the optimal value of the parameter D is found automatically by the program itself. The negative value of the vorticity parameter $C = -1$ indicates a high relative microrotation opposite to the macrorotation of the fault zone. As explained in Chapter 2, the value $C = -1$ indicates that blocks bounded by the fault planes did not rotate at all (they did not follow the macrorotation of the fault zone). According to Eq. (13), this also explains the symmetry of the stress tensor. The geometry of the observed fault system is very close to that predicted by the theory for the dominant optimal interacting fault subsystem (Fig. 5d).

8. Discussion

The classical continuum theory was used to explain the origin and tectonic interpretation of fault patterns characterized by kinematic interaction between the faults (Nieto-Samaniego and Alaniz-Alvarez, 1997). These authors tried to describe the formation of the fault-slip patterns, where the slip along two different faults is subparallel to their common intersection vector. In geomechanics, this type of faulting is well known as the wedge failure (e.g., Markland, 1972; Goodman, 1976; Yoon et al., 2002), and is extensively studied in the analysis of the rock slope stability. Nieto-Samaniego and Alaniz-Alvarez (1997) discovered that the wedge faulting characterized by kinematic interaction between the faults is the most probable cause for the formation of the multiple slip patterns on fault systems in the Earth's crust. Such fault systems are related to the reactivation of old pre-existing faults formed in previous tectonic phases. The authors also assumed that reactivated fault patterns with kinematic interaction do not reflect the symmetry of the strain or stress, because the reactivated faults and their cross-cutting relationships can have various orientations.

8.1. Intersecting faults in the classical continuum

The analyses described in this article reveal some new insights to the process of wedge faulting and the formation of the interacting fault systems. Contrary to the interpretation of Nieto-Samaniego and Alaniz-Alvarez (1997), our theoretical analysis and numerical tests show that the reactivated fault-slip patterns with kinematic interaction do reflect the symmetry of the strain or stress. In the classical (Cauchy) continuum there are two optimal orientations for the interacting systems of faults forming two optimal interacting subsystems. Both subsystems are aligned symmetrically with respect to the kinematic axes of the strain tensor. Each of them is characterized by its own intersection vector $\vec{d}_i$. The resolved shear and the resolved shear stress along all faults of the chosen subsystem are both parallel to the intersection vector $\vec{d}_i$. The orientations of the intersection vectors depend on the orientations of the kinematic axes of the instantaneous macrostrain tensor $\mathbf{u}^{(S)}$ and on the instantaneous deformation parameter D, which describes the shape of the instantaneous strain ellipsoid. The interaction is mathematically possible for all values of D, $0 \le D \le 1$. However, for $D = 0$ and $D = 1$ the mathematical results have no physical sense, because the shear stress along the faults is equal to zero.

8.2. Which faults can interact?

Both optimal interacting fault systems can consist of numerous faults. However, the interaction is only possible between pairs of faults with the unit normals $\vec{n}_i$ and $\vec{n}_j$ perpendicular to the common intersection vector $\vec{d}_i$ and at the same time the difference $\Delta\vec{n}_{ij} = \vec{n}_i - \vec{n}_j$ should be parallel to the relative microrotation $\vec{\phi}^{\mathrm{rel}}$. In nature, dispersions would most probably lead to interaction between arbitrary faults of the optimal interacting subsystem, because the slip direction is subparallel and interaction is kinematically possible as a movement of the block wedge bounded by the two fault planes. This is supported by the observations of the natural fault system in the Povodje quarry (Test 4, this article) and in the Peci quarry (Žalohar and Vrabec, 2010). In these fault systems, the slip directions are concentrated around the average common intersection direction among the observed faults. We believe that whenever the slip directions along two intersecting faults come close to their common intersection vector, it is most likely that the faults would interact. This would lead to the movement of the block wedge along the intersection line.

8.3. Intersecting faults in the Cosserat continuum

There exists a significant difference in geometry of interacting fault systems in the classical (Cauchy) continuum compared with the Cosserat continuum. First, the theory shows that the magnitude of the relative microrotation and asymmetry of the stress tensor have no effect (1) on the orientations of the faults belonging to the optimal interacting subsystems, and (2) on the slip orientation along these faults. Both, in the classical (Cauchy) and Cosserat continua, the direction of the intersection vector $\vec{d}$ depends only on the orientations of the kinematic axes of the instantaneous macrostrain tensor $\mathbf{u}^{(S)}$ (symmetric part, $\mathbf{e}^{(S)}$, of the Cosserat strain tensor, $\mathbf{e}$) and on the instantaneous deformation parameter D. Therefore the interacting fault subsystems predicted by the classical continuum (see Fig. 3) are also possible in the Cosserat continuum but are not symmetric (see Fig. 5), because the relative microrotation influences the magnitude of the resolved shear and resolved driving shear stress along the faults. This means that in the Cosserat continuum the two interacting subsystems do not accommodate the same amount of deformation. Depending on the magnitude of the relative microrotation $\vec{\phi}^{\mathrm{rel}}$, one of the optimal interacting subsystems is dominant over the other (it accommodates a larger amount of deformation), because the resolved driving shear stress along the faults belonging to the dominant subsystem is higher. In some cases, depending on the friction coefficient μ and values of the constitutive parameters p_r, a and b, the slip becomes impossible along the faults of the weaker (inferior) subsystem when the magnitude of the relative microrotation increases. In this case the total optimal interacting fault system is asymmetric and consists of a single optimal interacting subsystem.

8.4. Interpretation of the natural "optimal" interacting fault systems

The above discussion has important consequences for the interpretation of the fault-slip patterns in the Cosserat continuum. Theoretically, the relative microrotation does not affect the orientation of the resolved shear along the faults of the optimal interacting subsystems. Therefore, we could conclude that these subsystems contain little information on the Cosserat strain tensor and corresponding stress tensor. It is, however, interesting that in Test 4 the fault system observed in the Povodje quarry contained reliable information on the field of relative microrotation, although

the observed system has geometry very close to that predicted by the theory for the dominant optimal interacting subsystem. This can only be attributed to the strong dependence of the slip direction along the faults of the optimal interacting system on their orientations. As illustrated in Test 2, small changes in orientation of the chosen fault of the optimal interacting subsystem produce significant changes in the slip direction. The slip direction along the faults of the optimal interacting subsystems is highly numerically unstable. In the presence of natural noise, it remains close to the common intersection direction only for large relative microrotation. This means that in nature even the almost optimal interacting fault systems would contain reliable information on the field of the relative microrotation.

8.5. Interpretation of the natural "non-optimal" interacting systems

What the relative microrotation influences most is the slip direction along other non-optimally oriented faults that are geometrically not part of the optimal interacting subsystems and are not even close to it. We conclude that the diffusely orientated non-optimal faults contain the most of the information on the Cosserat strain and corresponding stress fields. The theory and tests show that the slip directions along the faults with the unit normal approximately perpendicular to the intersection vector belonging to the dominant optimal interacting subsystem also become subparallel to the common intersection vector of this subsystem. In nature, these non-optimal faults would probably interact with each other and also with the faults of the dominant optimal interacting subsystem forming even more complex and a highly asymmetrical fault system. The same is not true for the non-optimal faults with orientations close to the weaker optimal interacting subsystem. With the increasing relative microrotation the driving shear stress along these faults decreases and the probability for faults to slip also decreases. At the same time, the slip direction along these faults does not become subparallel to the intersection vector of the weaker optimal interacting subsystem.

The subspace of slip-capable orientations of the interacting non-optimal faults depends on the friction coefficient μ and asymmetry of the stress tensor defined by the value of the constitutive parameter b. For higher values of the friction coefficient and for lower values of the constitutive parameter b (symmetric stress) the subspace of slip-capable interacting non-optimal faults is confined closely around the vector $\vec{n}_0 = \vec{\lambda}_2 \times \vec{d}$. Note that $\vec{d}$ is the intersection vector of the dominant optimal interaction subsystem. For lower values of the friction coefficient and for more asymmetric stress tensors (larger values of the parameter b) the subspace of possible interacting fault orientations becomes broader. What Test 3 showed is that there exists a significant difference in the geometry of the non-optimal interacting fault system that can form in the symmetric and asymmetric stress. In the asymmetric stress there exist numerous fault planes subparallel to the maximum kinematic axis $\vec{\lambda}_1$ of the instantaneous macrostrain tensor $\underline{\mathbf{u}}^{(S)}$. The orientation of slip along such faults is also subparallel to $\vec{\lambda}_1$. In the symmetric stress these fault planes are impossible to slip.

Observations described by Žalohar and Vrabec (2010) and in this article (Test 4) showed that fault systems very similar to those predicted by the theory exist in nature. It was also shown that they contain reliable information on the relative microrotation field in the time of faulting.

9. Conclusions

1. The classical continuum theory is capable of describing interaction between intersecting faults producing slip direction to be subparallel to the common intersection direction among the faults. In the classical continuum, there exist two optimal interacting subsystems with symmetrical orientations with respect to the strain or stress axes. The orientations of the optimal interacting subsystems depend on the orientations of the kinematic axes of the instantaneous macrostrain tensor and on the instantaneous deformation parameter D, which describes the shape of the instantaneous strain ellipsoid.
2. These optimal interacting subsystems consist of numerous differently orientated pairs of faults all having the same direction of slip. Movement along the intersection line among a pair of interacting faults leads to the wedge failure/faulting.
3. In the Cosserat continuum both optimal interacting subsystems predicted by the classical theory are also possible but are not symmetric. Because the relative microrotation has a considerable effect on the magnitude of the resolved shear and resolved driving shear stress, one of the optimal interacting subsystems becomes dominant and accommodates a larger amount of deformation than the other (the weaker subsystem). In some cases, the Cosserat continuum is characterized by a single optimal interacting subsystem, which depends (1) on the friction coefficient, (2) on the constitutive parameters describing the stress–strain relationship, and (3) on the magnitude of the relative microrotation.
4. In the case of high relative microrotation, numerous non-optimal faults with the unit normal approximately perpendicular to the intersection vector belonging to the dominant optimal interacting subsystem also have the slip direction subparallel to the intersection vector of the dominant optimal interacting subsystem. These non-optimal faults would most probably interact with each other and with faults of the dominant optimal interacting subsystem, thus forming an even more complex and asymmetrical interacting system of faults.
5. Whenever fault systems observed in nature indicate wedge faulting, the classical methods for fault-slip data analysis are unsuitable. The Cosserat methods should be used instead. Numerical tests (e.g., Test 4) demonstrate that the Cosserat continuum theory predicts remarkably similar fault system geometry that can sometimes be actually observed in nature.

Acknowledgments

The author is grateful to professor Robert J. Twiss who performed a very detailed review of the manuscript and contributed many constructive comments and ideas that helped to improve its quality. Many thanks also to the unknown anonymous reviewer and to the editor Tom G. Blenkinsop for his thorough editorial handling. The author also greatly appreciates many useful comments given by professor Will Tomford, who helped to improve the language of the manuscript.

References

Besdo, D., 1974. Ein Beitrag zur nichtlinearen Theorie des Cosserat-Kontinuums. Acta Mechanica 20, 105–131.
Besdo, D., 1985. Inelastic behavior of plane frictionless block-systems described as Cosserat media. Archive of Mechanics 37, 603–619.
Cosserat, E., Cosserat, F., 1909. Théorie des Corps Déformables. Hermann et Fils, Paris.
Dartevelle, S., 2003. Numerical and granulometric approaches to geophysical granular flows. Ph.D. thesis. Michigan Technological University, Michigan.
de Borst, R., 1991. Simulation of strain localization: a reappraisal of the Cosserat continuum. Engineering Computations 8, 317–332.
de Borst, R., 1993. A generalization of J2-flow theory for polar continua. Computer Methods in Applied Mechanics and Engineering 103, 347–362.
Eringen, A.C., 1968. Theory of micropolar elasticity. In: Liebowitz, H. (Ed.), Fracture II. Academic Press.
Eringen, A.C., 1999. Microcontinuum Field Theories. Springer, New York.
Eringen, A.C., 2002. Nonlocal Continuum Field Theories. Springer, New York.
Eringen, A.C., Suhubi, E.S., 1964. Nonlinear theory of simple microelastic solids. International Journal of Engineering Science 2, 189–203. 389–404.

Etse, G., Nieto, M., 2004. Cosserat continua-based micro plane modeling. Theory and numerical analysis. Latin American Applied Research 34, 229–240.
Figueiredo, R.P., Vargas, E.A., Moraes, A., 2004. Analysis of bookshelf mechanisms using the mechanics of Cosserat generalized continua. Journal of Structural Geology 26, 1931–1943.
Forest, S., 2000. Cosserat media. In: Buschow, K.H.J., Cahn, R.W., Flemings, M.C., Ilschner, B., Kramer, E.J., Mahajan, S. (Eds.), Encyclopedia of Materials: Science and Technology. Elsevier Science Ltd, pp. 1715–1718.
Forest, S., Sievert, R., 2003. Elastoviscoplastic constitutive frameworks for generalized continua. Acta Mechanica 160, 71–111.
Forest, S., Barbe, F., Cailletaud, G., 2000. Cosserat modeling of size effects in the mechanical behaviour of polycrystals and multi-phase materials. International Journal of Solids and Structures 37, 7105–7126.
Forest, S., Cailletaud, G., Sievert, R., 1997. A Cosserat theory for elastoviscoplastic single crystals at finite deformation. Archive of Mechanics 49, 705–736.
Forest, S., Pradel, F., Sab, K., 2001. Asymptotic analysis of heterogeneous Cosserat media. International Journal of Solids and Structures 38, 4585–4608.
Germain, P., Nguyen, Q.S., Suquet, P., 1983. Continuum thermodynamics. Journal of Applied Mechanics 50, 1010–1020.
Goodman, R.E., 1976. Methods of Geological Engineering in Discontinuous Rocks. West Publishing, San Francisco.
Grad, K., Ferjančič, L., 1968. Basic Geologic Map of the SFRJ 1: 100.000, Sheet Kranj. Zvezni Geološki Zavod, Beograd.
Hansen, E., Willam, K., Carol, I., 2001. A two-surface anisotropic damage/plasticity model for plain concrete. In: de Borst, R. (Ed.), Proceedings of Framos-4 Conference Paris, May 28–32, 2001, Fracture Mechanics of Concrete Materials. A.A. Balkema, Rotterdam, pp. 549–556.
Kröner, E., 1968. Mechanics of generalized continua. In: Proceedings of IUTAM Symposium. International Union of Theoretical and Applied Mechanics, Springer-Verlag, Berlin.
Lemaitre, J., Chaboche, J.-L., 1994. Mechanics of Solid Materials. Cambridge University Press.
Lippmann, H., 1969. Eine Cosserat – Theorie des Plastischen Fliens. Acta Mechanica 8, 255–284.
Manzari, M.T., 2004. Application of micropolar plasticity to post failure analysis in geomechanics. International Journal for Numerical and Analytical Methods in Geomechanics 28, 1011–1032.
Markland, J.T., 1972. A Useful Technique for Estimating the Stability of Rock Slopes When the Rigid Wedge Sliding Type of Failure is Expected. Imperial College Rock Mechanics. Research Report 19.
Mindlin, R.D., 1964. Micro-structure in linear elasticity. Archive for Rational Mechanics and Analysis 16, 51–78.
Mohan, L.S., Nott, P.R., Rao, K.K., 1999. A frictional Cosserat model for the flow of granular materials through a vertical channel. Acta Mechanica 138, 75–96.
Mühlhaus, H.-B., Vardoulakis, J., 1987. The thickness of shear bands in granular materials. Géotechnique 37, 271–283.
Nieto-Samaniego, A.F., Alaniz-Alvarez, S.A., 1997. Origin and tectonic interpretation of multiple fault patterns. Tectonophysics 270, 197–206.
Placer, L., 1999. Contribution to the macrotectonic subdivision of the border region between Southern Alps and External Dinarides. Geologija 41, 223–243.
Premru, U., 1983a. Basic Geological Map of Yugoslavia, 1: 100000, Sheet Ljubljana. Zvezni Geološki Zavod, Beograd.
Premru, U., 1983b. Basic Geological Map of Yugoslavia, 1: 100000, Guidebook of the Sheet Ljubljana. Zvezni Geološki Zavod, Beograd.
Salari, M.R., Saeb, S., Willam, K., Patchet, S.J., Carrasco, R.C., 2004. A coupled elastoplastic damage model for geomaterials. Computer Methods in Applied Mechanics and Engineering 193, 2625–2643.
Sawczuk, A., 1967. On yielding of Cosserat continua. Archive of Mechanics 19, 3–19.
Toupin, R.A., 1962. Elastic materials with couple stresses. Archive for Rational Mechanics and Analysis 11, 385–414.
Toupin, R.A., 1964. Theories of elasticity with couple-stress. Archive for Rational Mechanics and Analysis 17, 85–112.
Twiss, R.J., 2009. An asymmetric micropolar moment tensor derived from a discrete-block model for a rotating granular substructure. Bulletin of the Seismological Society of America 99 (2B), 1103–1131.
Twiss, R.J., Unruh, J.R., 1998. Analysis of fault slip inversions: do they constrain stress or strain rate? Journal of Geophysical Research 103, 12205–12222.
Twiss, R.J., Unruh, J.R., 2007. Structure, deformation and strength of the Loma Prieta fault, northern California, USA, as inferred from 1989–1990 Loma Prieta aftershock sequence. GSA Bulletin 119, 1079–1106.
Twiss, R.J., Protzman, G.M., Hurst, S.D., 1991. Theory of slickenline patterns based on the velocity gradient tensor and microrotation. Tectonophysics 186, 215–239.
Twiss, R.J., Souter, B.J., Unruh, J.R., 1993. The effect of block rotations on the global seismic moment tensor and patterns of seismic P and T axes. Journal of Geophysical Research 98, 645–674.
Unruh, J.R., Twiss, R.J., Hauksson, E., 1996. Seismogenic deformation field in the Mojave block and implications for tectonics of the eastern California shear zone. Journal of Geophysical Research 101 (B4), 8335–8361.
Willam, J.K., 2002. Constitutive models for engineering materials. In: Encyclopedia of Physical Science and Technology, third ed., vol. 3. Academic Press, pp. 603–633.
Yoon, W.S., Jeong, U.J., Kim, J.H., 2002. Kinematic analysis for sliding failure of multifaced rock slopes. Engineering Geology 67, 51–61.
Žalohar, J., Vrabec, M., 2007. Paleostress analysis of heterogeneous fault-slip data: the Gauss method. Journal of Structural Geology 29, 1798–1810.
Žalohar, J., Vrabec, M., 2008. Combined kinematic and paleostress analysis of fault-slip data: the multiple-slip method. Journal of Structural Geology 30, 1603–1613.
Žalohar, J., Vrabec, M., 2010. Kinematics and dynamics of fault reactivation: the Cosserat approach. Journal of Structural Geology 32, 15–27.